

Dated: 29 December 2021

The Virgo Collaboration + additional authors

. To be submitted to CQG

Virgo INTERNAL DOCUMENT – NOT FOR PUBLIC DISTRIBUTION

The Virgo O3 run and the impact of the environment

The Virgo Collaboration + a few additional authors

Abstract. Sources of geophysical noise (such as wind, sea waves and earthquakes) or of anthropogenic noise impact ground-based gravitational-wave interferometric detectors, causing transient sensitivity worsening and gaps in data taking. During the one year-long third Observing Run (O3: from April 01, 2019 to March 27, 2020), the Virgo Collaboration collected a statistically significant dataset, used in this article to study the response of the detector to a variety of environmental conditions. We correlated environmental parameters to global detector performance, such as observation range, duty cycle and control losses. Where possible, we identified weaknesses in the detector that will be used to elaborate strategies in order to improve Virgo robustness against external disturbances for the next data taking period, O4, currently planned to start at the end of 2022. The lessons learned could also provide useful insights for the design of the next generation of ground-based interferometers.

17 **Contents**

18 **1 Introduction** **3**

19 **2 The Virgo environmental monitoring during O3** **5**

20 **3 Seismic noise** **6**

21 3.1 The seismic frequency bands and their evolution during the O3 run . . . 7

22 3.2 Impact on the Virgo detector 11

23 3.2.1 Sensitivity 11

24 3.2.2 Duty cycle 12

25 **4 Earthquakes** **13**

26 4.1 O3 Seismon setup at EGO 15

27 4.2 Earthquakes impact during O3 16

28 4.3 Plans for O4 21

29 **5 Bad weather** **22**

30 5.1 Impact of sea activity 22

31 5.1.1 Microseism impact on strain noise 23

32 5.1.2 Microseism impact on glitch rates 24

33 5.1.3 Microseism and scattered light 25

34 5.1.4 Identification of scattered light culprits 27

35 5.2 Impact of wind 28

36 5.3 Disentangling sea activity and wind 30

37 **6 Other environment impacts** **31**

38 6.1 Magnetic noise 31

39 6.2 Lightnings 33

40 6.3 Cosmic muons 34

41 **7 Outlook and prospects for O4** **35**

42 **Appendix A Study of the control losses during O3** **37**

43 1. Introduction

44 The past decade has seen the ramp-up of the second-generation ('Advanced') earth-based
45 gravitational-wave (GW) detectors. Design improvements and technological upgrades
46 have paved the way to the first direct detections of GWs by the global network made up
47 of the two aLIGO instruments [1] (located in the USA: Hanford, WA and Livingston,
48 LA) and of the Advanced Virgo detector [2] (located in Cascina, Italy). The main
49 results achieved by the LIGO Scientific Collaboration and the Virgo Collaboration –
50 recently joined by the KAGRA collaboration whose detector [3], located under the
51 Kamioka mountain in Japan, is nearing completion – include the first detection of
52 a binary black hole merger (GW150914 [4]); the first detection of a binary neutron
53 star merger (GW170817 [5]) that lead to the birth of multi-messenger astronomy with
54 GW [6]; and now dozens of detections of compact binary mergers that add up in a GW
55 Transient Catalogue regularly updated [7, 8, 9]. These detections contribute to opening
56 a new window onto the Universe by providing insights to the populations of compact
57 objects and the binary merger rates [10]; they also allow scientists to perform stringent
58 tests of general relativity [11] in a new regime of gravitation never probed before.

59 The operation of ground-based GW detectors is organized into successive steps forming a
60 recurring sequence over the years: upgrades; commissioning and sensitivity improvement
61 (the so-called *noise hunting* phase); data-taking periods called observing runs (or simply
62 runs and labelled *On*). So far there have been three runs for the global network of
63 advanced detectors.

- 64 • O1 (09/2015 – 01/2016) with only the two LIGO detectors taking data;
- 65 • O2 (11/2016 – 08/2017) with Virgo joining LIGO on August 01, 2017;
- 66 • finally O3 (04/2019 – 03/2020), that saw the three detectors take data jointly
67 during 11 months in total: 6 months first (a run called O3a), followed by a 1-month
68 break (October 2019) and then another period of 5 months of data taking (O3b),
69 interrupted about a month earlier than expected due to the worldwide COVID-19
70 pandemic.

71 The above listing shows that the O3 run was the first *long* data-taking period for the
72 Advanced Virgo detector. Therefore, we have used the wealth of unprecedented data
73 collected during this year to make an in-depth analysis of the instrument performance.
74 In this article, we study the impact of the environment on Advanced Virgo, along the
75 lines of previous publications from Virgo [12], LIGO [13] or KAGRA [14]. We focus on
76 various types of seismic noises, on earthquakes and on bad weather periods. We also
77 briefly investigate the effect of other possible disturbances: magnetic noise, lightning
78 and cosmic muons. Our goal is threefold: to quantify how the Virgo sensitivity and
79 duty cycle depend on these external parameters; to use this knowledge to prepare the
80 next run, O4, scheduled to start in the second semester 2022; finally, to build experience
81 for future GW detectors, in particular for the Einstein Telescope project [15].

82 The Virgo detector is located in Italy at EGO, the European Gravitational Observatory,
83 in the municipality of Cascina. The EGO site is in the countryside, about 12 km south-
84 east of Pisa and about 17 km east of the Tyrrhenian coast. Virgo is not far from some
85 industrial and commercial sites that can generate noise. Within 7 km from EGO there
86 are: elevated highways, railway tracks, wind turbines, earth quarries, electroducts and
87 the Pisa airport. To avoid pressure waves potentially shaking the ground, a no-fly zone
88 has been enforced in a cylindrical volume (600 m radius and height) above each of the
89 Virgo experimental buildings.

90 Advanced Virgo is a power-recycled Michelson interferometer with Fabry-Perot cavities
91 in its 3 km-long arms. All core optics are suspended to long suspensions, called the
92 superattenuators [16], that have a twofold use: first, to isolate as much as possible the
93 mirrors from seismic motions (both vertical and longitudinal), and then to control very
94 accurately their positions in all six degrees of freedom. Many feedback systems are used
95 to bring the detector to its working point and maintain it there [17, 18]. This state – the
96 same for O2 and O3: the Michelson interferometer on a dark fringe, the Fabry-Perot and
97 power recycling cavities in resonance – is the only one in which the detector is sensitive
98 to the passing of GWs.

99 During a run, priority is obviously given to taking data of quality good enough to be
100 included in physics analysis. In that case, Virgo is said to be in *Science mode*. During
101 O3, the average duty cycle in Science mode has been around 76% [19], with the remaining
102 time almost equally divided into three categories.

- 103 • Control acquisition and adjustment phases, to restore the working point and restart
104 taking data in Science mode;
- 105 • Recurring controlled actions on the detector: maintenance (usually a few hours
106 on Tuesday mornings local time), calibration (usually every Wednesday evening)
107 or commissioning (measurements, working point tuning or tailored improvements:
108 sessions organized when the need arises);
- 109 • Problems preventing a smooth running of the detector.

110 The article is organized as follows. Section 2 describes the environmental monitoring
111 of the Virgo detector during the O3 run. Section 3 is dedicated to the different seismic
112 noise contributions (either natural or human-related): how to disentangle them, how
113 to monitor them and what their impacts on the detector are in terms of sensitivity
114 and duty cycle. Section 4 provides an analysis of the impact of earthquakes on the
115 detector. Section 5 studies the impact of bad weather on data quality and duty cycle,
116 disentangling contributions from sea activity and wind. Section 6 goes through other
117 environment impacts: magnetic noise, lightning and a study of the cosmic muon rate on
118 the Virgo central building. Then, Section 7 concludes this article by opening outlooks
119 to the future O4 run. Finally, Appendix A provides a detailed and quite complete
120 classification of the control losses during the O3 run. Although that study has a scope

broader than the present article, it is included here for reference and also because its results were used, in particular to find out which control losses were due to earthquakes.

2. The Virgo environmental monitoring during O3

The Virgo detector is equipped with a large set of probes used to monitor the conditions of the surrounding environment. Since these conditions can influence the detector response, or even mimic a GW event, it is very important to track their evolution, to assess the right working condition of the detector or to use them as veto against possible fake signals.

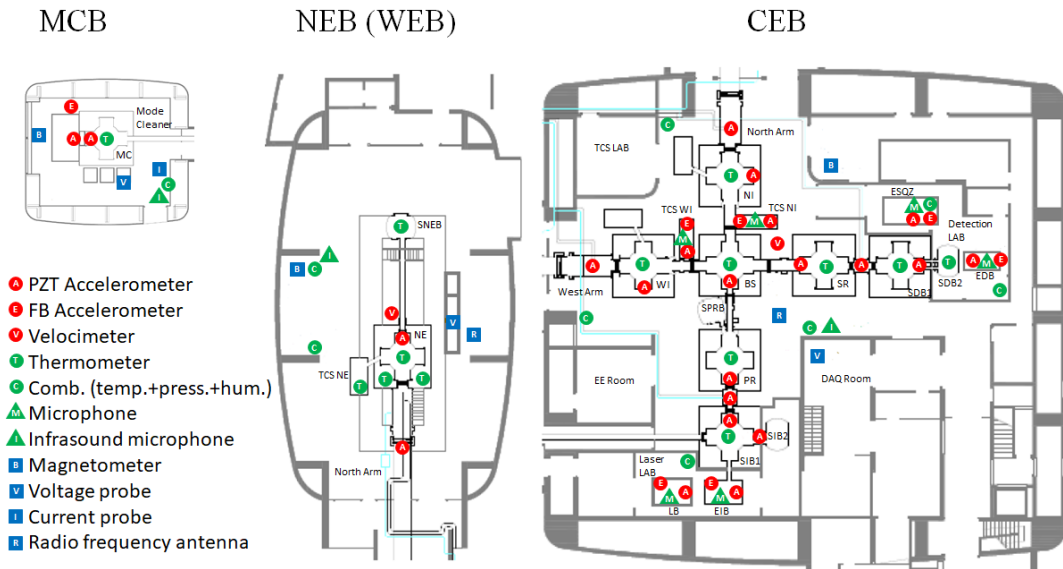


Figure 1: Location of the probes used for the Virgo environmental monitoring system. Maps of most relevant building are shown: left MCB, middle NEB, right CEB. The WEB is very similar to NEB and is not shown.

The set of probes and their conditioning electronics constitute the Environmental Monitoring System (EMS). The EMS was initially composed by a few tens of environmental probes (EPs) [20] and then improved during the detector upgrades that occurred in the past years. During O3, the total number of channels belonging to EMS was about 420.

The EMS is also helpful to understand the origin of some noise sources affecting the detector sensitivity. Indeed it was largely used during the commissioning phase following each detector upgrade, to recover and improve the Virgo performance in terms of sensitivity and duty cycle [12].

Data acquired for EMS can be grouped in two classes depending on the sample rate used for the different EPs. High-rate, or fast class, includes those EPs acquired at rate up to 20 kHz like seismometers, piezoelectric (PZT) accelerometers, force balance

141 (FB) accelerometer, magnetometers, microphones, voltage and current sensors, radio-
 142 frequency (RF) antennas, while low-rate or slow class includes temperature, pressure,
 143 humidity, weather and lightning probes, acquired at 1 Hz rate.

Type	Model	Frequency Band
Seismometer	Guralp CMG-40T	0.01 – 50 Hz
FB Accelerometer	Kinematics FBA ES-T	0.1 – 200 Hz
PZT Accelerometer	Wilcoxon 731-207 or PCB 393B12	1 Hz – 1 kHz
Magnetometer	Metronics MFS-06 or MFS-06e	0.1 mHz – 10 kHz
Microphone	Brüel & Kjær 4190 or 4193	0.1 – 10 kHz
RF antenna	AAS STA 5 A/D/0.01-100	10 kHz – 100 MHz
Voltage probe	Talema 0015P1-2-009	DC – 10 kHz
Current probe	IME 0015P1-2-009	DC – 10 kHz
Temperature probe	Analog Device AD590	DC – 0.5 Hz
Humidity probe	Honeywell HIH-5031-001	DC – 0.5 Hz
Pressure probe	NXP MPXA4115A6U	DC – 0.5 Hz
Weather station	Davis Advantage Pro 2	DC – 0.3 Hz
Lightning detector	Boltek LD 250	DC – 0.5 Hz

Table 1: Characteristics of the Virgo environmental probes used during O3.

144 The main characteristics (type, model and frequency band) of the EPs in use during O3
 145 are listed in Table 1. Figure 1 shows the arrangement of the EPs inside the main Virgo
 146 buildings. Most probes are located in the experimental halls of the relevant buildings
 147 of the detector: Central Building (CEB), North and West End Buildings (NEB and
 148 WEB) and Mode Cleaner Building (MCB). Usually, the probes are in contact with
 149 critical elements of the detector, like the walls of the vacuum chambers containing
 150 the test mass suspensions, or the optical benches hosting the laser injection and GW
 151 detection systems. Figure 2 shows a bird eye's view of the Virgo detector at EGO, with
 152 an emphasis on the location of the buildings that are identified in this article.

153 Few probes are placed outside the buildings and are not shown in the schematics, namely
 154 the weather station, the lightning detector and two additional magnetometers. These
 155 two low-noise induction coil magnetometers are deployed at 0.5 m depth in the soil, at
 156 about 100 m from the CEB, oriented along the geographic North and West directions.
 157 Their data are shared in real time with the EM antenna network "Radio waves below
 158 22 kHz" [21].

159 3. Seismic noise

160 In this section we introduce the main sources of seismic noise at EGO. They are
 161 disentangled and monitored by examining seismic probes in specific frequency bands.

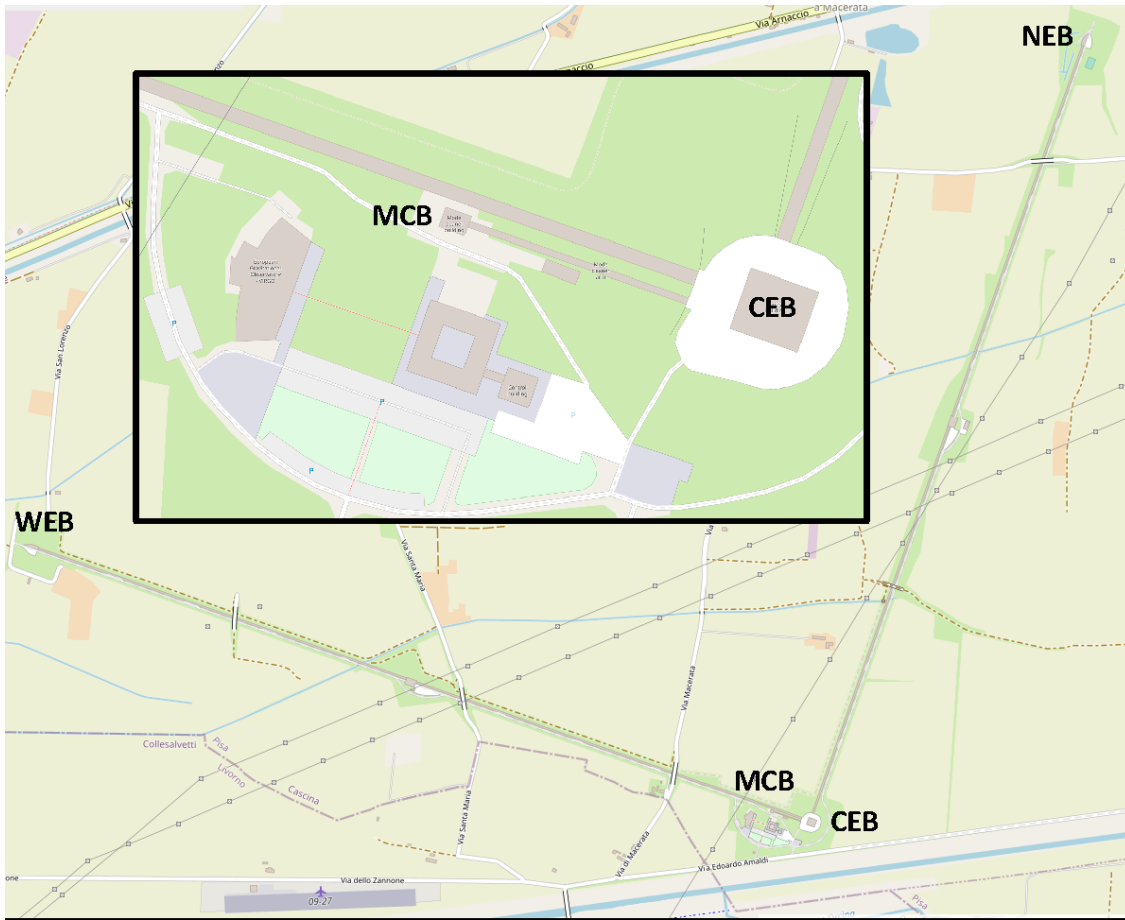


Figure 2: Map [22] of the EGO site showing the Virgo detector and in particular the location of the main buildings identified in the text. The central insert shows a zoom around the interferometer vertex, with the CEB and MCB highlighted. The Mode-Cleaner cavity is 144 m-long, while the Virgo arms are 3-km long.

162 We provide a statistical description of the noise and evidence its main recurring features.
 163 Then, we describe how they impacted on the detector during the O3 run.

164 3.1. The seismic frequency bands and their evolution during the O3 run

165 The seismic wavefield at EGO, the site of the Virgo detector, is the sum of several
 166 sources [24]. Seismic spectrum variability during the O3 run is illustrated in Fig. 3. The
 167 largest contribution to seismic ground motion in the frequency range between 0.1 Hz
 168 and 1 Hz, referred to as *microseism*, is due to the interaction between shallow water sea
 169 waves and the bottom of the sea [25, 26]. At EGO, the prevailing microseismic peak is
 170 around 0.35 Hz.

171 Figure 4 shows the time evolution of microseism during the O3 run, while Fig. 5 shows
 172 the corresponding cumulative distribution, split by season. Microseism intensity follows
 173 seasonal variations, being larger in fall and winter, due to the stronger wind and sea

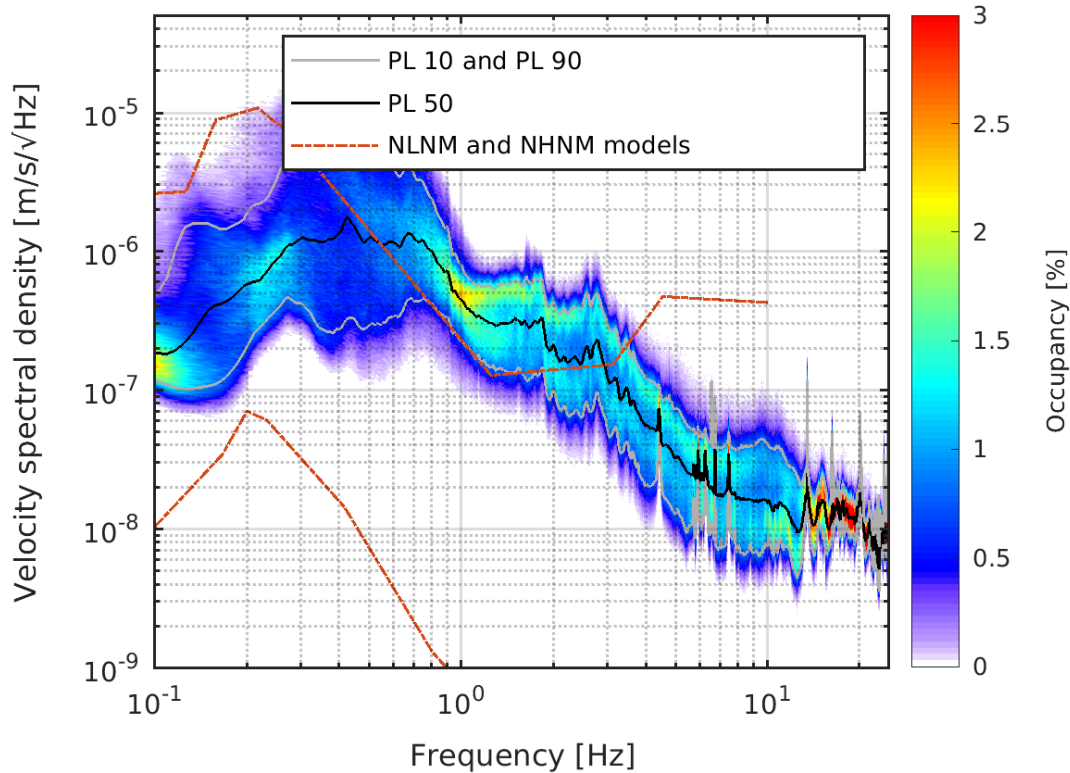


Figure 3: Variability of horizontal velocity of the Virgo NEB ground floor during O3. The quantity shown is the 2D histogram of the E-W velocity amplitude spectral density computed for the whole dataset recorded during O3 divided into 128 second long chunks. All interferometer maintenance periods are excluded from the computation. The color scale indicates the percent occupancy of histogram bins. The superposed continuous curves show different percentile levels (labelled *PL* on the plot): 10% (gray), 50% (black) and 90% (gray as well). The two red dashed curves correspond to the Peterson low-noise ('NLNM') and high-noise ('NHHM') models [23].

174 activity.

175 Above 1 Hz, anthropogenic sources dominate the spectrum. Heavy vehicles (trucks and
 176 alike) on ~ 1 km distant elevated roads are the prevailing source of seismic noise in the
 177 1-10 Hz band [24].

178 As illustrated in Fig. 6, the RMS of seismic noise in the 1-5 Hz band follows a working
 179 day/night cycle with higher levels during working hours (from 8:00 to 17:00 local time –
 180 LT), with small reduction during lunch break (12:00-14:00 LT) and minima during week-
 181 ends and holidays. The blue curve, used as reference, covers the whole O3 run. The
 182 green curve is based on a 4-week period, from Monday 16 December, 2019 to Sunday 12
 183 January, 2020: the noise reduction during the two consecutive Wednesdays, Christmas
 184 2019 and the New Year's Day 2020, is quite impressive. A significant reduction of the
 185 anthropogenic noise is also visible during the Spring 2020 lockdown in Italy, due to the

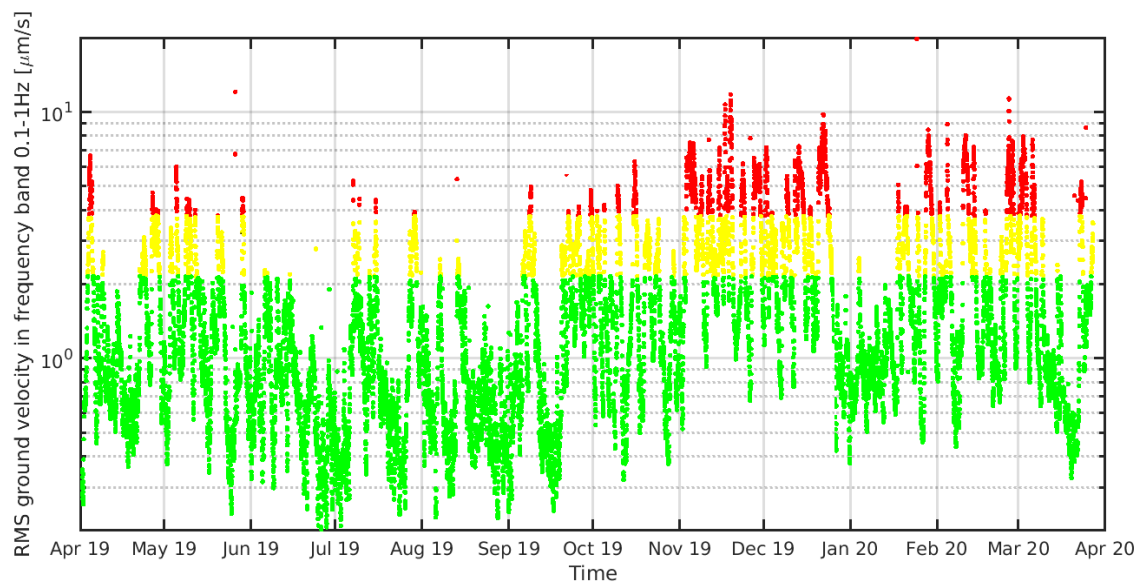


Figure 4: Evolution during O3 of seismic RMS in the 0.1 to 1 Hz frequency band. Data colored in yellow and red exceed the 75th and 90th percentile, respectively.

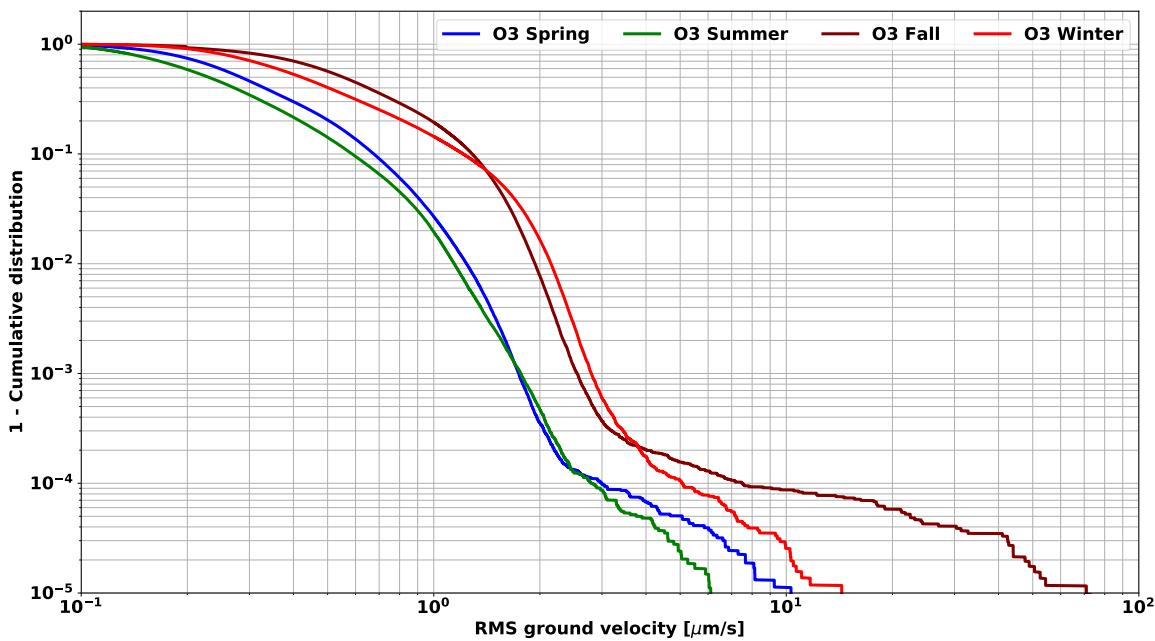


Figure 5: Cumulative distribution of microseism in the frequency band 0.1-1 Hz (dominated by sea activity), measured at EGO during each season in 2019-2020.

186 COVID-19 pandemic (red curve, covering a 8-week period from 09 March to 03 May).
 187 That decrease is smaller than for the Christmas and New Year holidays but it is more
 188 global as it is visible for all days of the week.

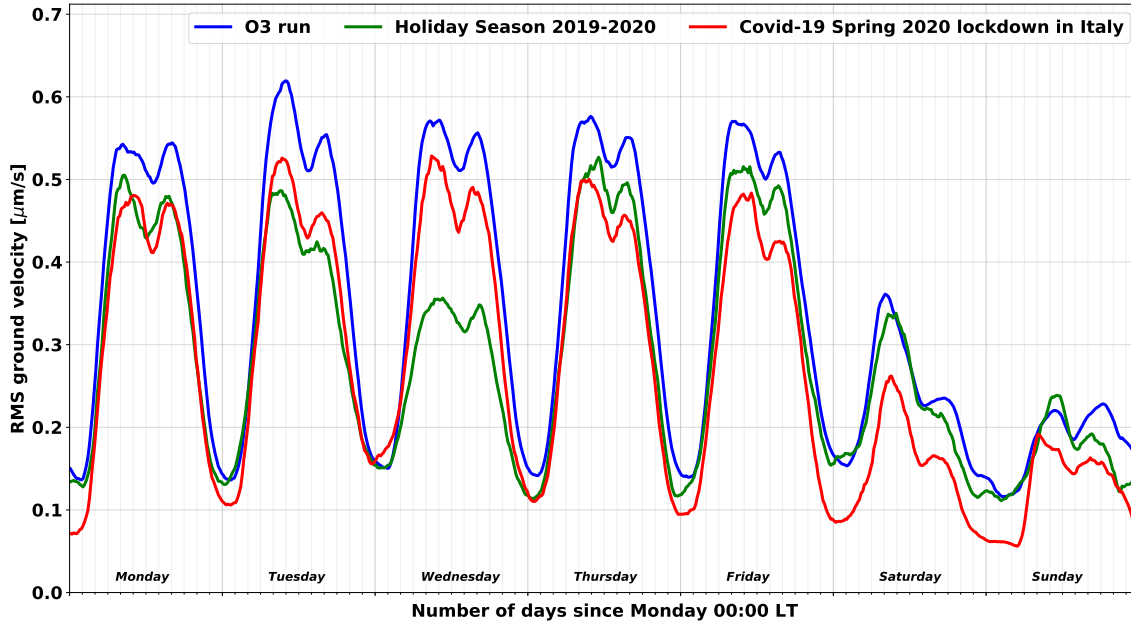


Figure 6: Average evolution on a weekly basis of the seismic anthropogenic noise (frequency band: 1-5 Hz) measured at EGO during different times in 2019-2020.

189 Finally, above 10 Hz, the dominant seismic contribution is generated locally: vehicles in
 190 nearby and on-site roads, agricultural work on neighbouring land, etc. Figure 7 shows
 191 the average day-night variations, computed in the 10-40 Hz band on a weekly basis: in
 192 blue during the O3 run; in magenta during the 1-month commissioning break (October
 193 2019) separating the two halves of O3; finally in orange for the second semester of
 194 2020, during which hardware upgrades and construction or infrastructure works for the
 195 Advanced Virgo+ project [27] took place.

196 The common feature between the three curves is the dominant peak on Tuesday
 197 mornings, the usual slot used for the weekly maintenance of the Virgo detector. This
 198 activity includes in particular the refilling of Nitrogen[‡] tanks by heavy trucks coming on-
 199 site, and the possibility to have people moving around and working inside experimental
 200 areas whose access is forbidden during data taking periods. The on-site seismic noise
 201 level was slightly higher during the commissioning break compared to the O3 run, but
 202 not by much: that 1-month shutdown was not long enough to allow for invasive works
 203 that could have jeopardized the restart of data taking on November 01, 2019, alongside
 204 the two LIGO detectors. On the other hand, on-site activities are more evenly distributed
 205 over working days during the post-O3 upgrade. Though, activities were the lowest on

[‡] Liquid Nitrogen is used to cool down the Advanced Virgo cryotrap [2].

206 weekends during that period because of site access restrictions, enforced because of the
 207 pandemic.

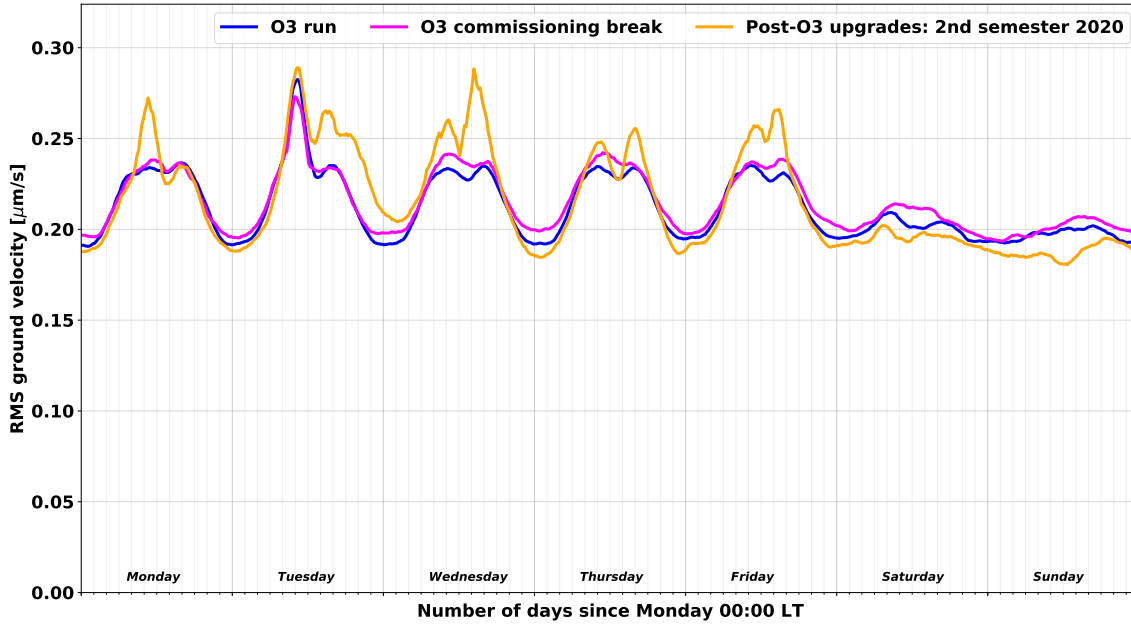


Figure 7: Average evolution on a weekly basis of the seismic on-site noise (frequency band: 10-40 Hz) measured at EGO during different times in 2019-2020.

208 3.2. Impact on the Virgo detector

209 The previous sections have demonstrated that the Virgo collaboration is accurately
 210 monitoring the seismic environment at EGO and that the recorded data show significant
 211 variations over time, in agreement with expectations from known noise sources. It is
 212 then interesting to see how these noises impact the performance of the Virgo detector,
 213 namely its sensitivity and duty cycle.

214 *3.2.1. Sensitivity* A convenient way to monitor the sensitivity of a gravitational-wave
 215 detector like Virgo is to study the evolution of the *BNS range*, that is the average
 216 distance up to which the merger of a standard binary neutron star system (BNS) can
 217 be detected with a signal-to-noise ratio (SNR) set to 8, roughly corresponding to one
 218 false alarm per year with purely Gaussian noise. The average is taken over the position
 219 of the BNS in the sky and over the orientation of its orbital plane. Broadly speaking,
 220 the lower (higher) the noise in the frequency band of interest –from a few tens of Hz to
 221 a few hundreds of Hz depending on the actual sensitivity curve –, the larger (smaller)
 222 the BNS range.

223 In addition to its potential dependence on the surrounding environment, the BNS range
 224 can fluctuate significantly due to changes in the control accuracy of the detector.
 225 Therefore, averaging raw BNS range values, especially over long timescales, is not
 226 expected to provide meaningful information as one would mix together too many effects
 227 that cause the BNS range to vary. Therefore, the method used in the following consists in
 228 computing a moving daily average of the BNS range and to focus on the local fluctuations
 229 around this level. Figures 8 and 9 show these variations, averaged over the whole O3
 230 run, and projected over a weekly or daily time range, respectively. On both plots, the
 231 red dots show daily variations while the blue curve is a moving median profile of the
 232 scatter plot. The variations seen are clearly of anthropogenic origin, with a day-night
 233 pattern and a reduced spread during the weekend. Although they are significant, they
 234 are also limited in size: ~ 1 Mpc compared to an average BNS range of about 50 Mpc
 235 during the O3 run, hence a $\sim 2\%$ fluctuation. This shows the robustness of the Virgo
 236 detector.

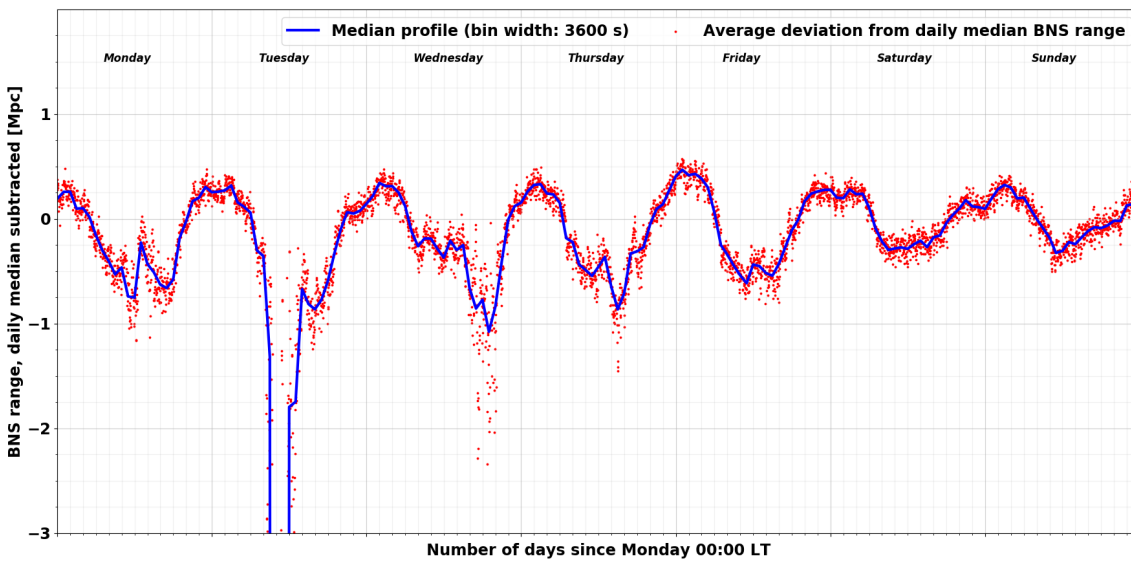


Figure 8: Average variation of the BNS range around its local average, computed on a weekly basis. The blue trace is a moving median profile of the red scatter plot, each dot showing the fluctuation at a particular weekday and time. The lack of available data on Tuesday morning corresponds to the weekly maintenance period of the Virgo detector, while the sharper variations on Wednesday and Thursday afternoons are due to the fact that these times have often been used for calibration or detector activities. Therefore, the BNS range is less stable than usually when nominal data taking gets restored.

237 *3.2.2. Duty cycle* Figure 10 shows the average duty cycle of the Virgo detector during
 238 the O3 run. The top plot displays its average variation over a week, while the bottom one
 239 focuses on a day. The red curve normalizes the Science mode data taking by the elapsed

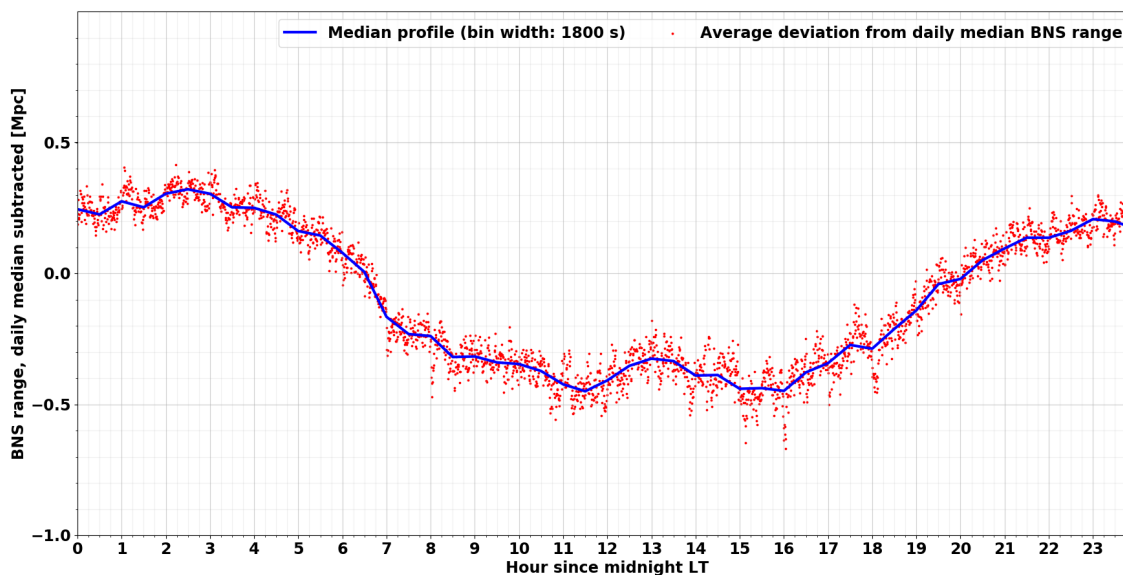


Figure 9: Average variation of the BNS range around its local average, computed on a daily basis. The blue trace is a moving median profile of the red scatter plot, each dot showing the fluctuation at a particular time of the day.

240 real time, while the green one is computed by excluding the calibration, commissioning
 241 and maintenance periods. Thus, the latter curve shows the fraction of the time available
 242 for data taking that is actually used for that. Activities on the detector are concentrated
 243 during working hours as expected, with maintenance on Tuesday morning, calibrations
 244 on Wednesday evenings and commissioning slots from Monday to Friday depending on
 245 the needs. There is a non-negligible recovery time from maintenance, while the transition
 246 from calibration back to data taking is smoother and quicker on average. During the
 247 quietest hours of the night, when no work takes place on the interferometer except in
 248 case of an emergency, the average duty cycle reaches a plateau around 85%.

249 4. Earthquakes

250 Earthquakes radiate energy through different types of seismic waves that are commonly
 251 divided in "body" and "surface" waves, depending on the path followed from the source
 252 to the receiver. Body waves that travel through the Earth are usually detected first. The
 253 fastest are named P-waves and are compressional longitudinal waves whose speed can
 254 reach 8 km/s. Then come the S-waves, transverse shear waves whose velocity scales by a
 255 factor of $\sqrt{2}$ with respect to P-waves. Surface waves are slower and their size dominates
 256 at large epicentral distance since their amplitude scaling factor is $1/\text{distance}$ while body
 257 waves scale with $1/\text{distance}^2$. Most relevant surface waves are Rayleigh waves, that
 258 originate from P-wave and S-wave (with vertical polarization) coupling at the Earth
 259 surface. The result is a wave with both longitudinal and transversal components and a

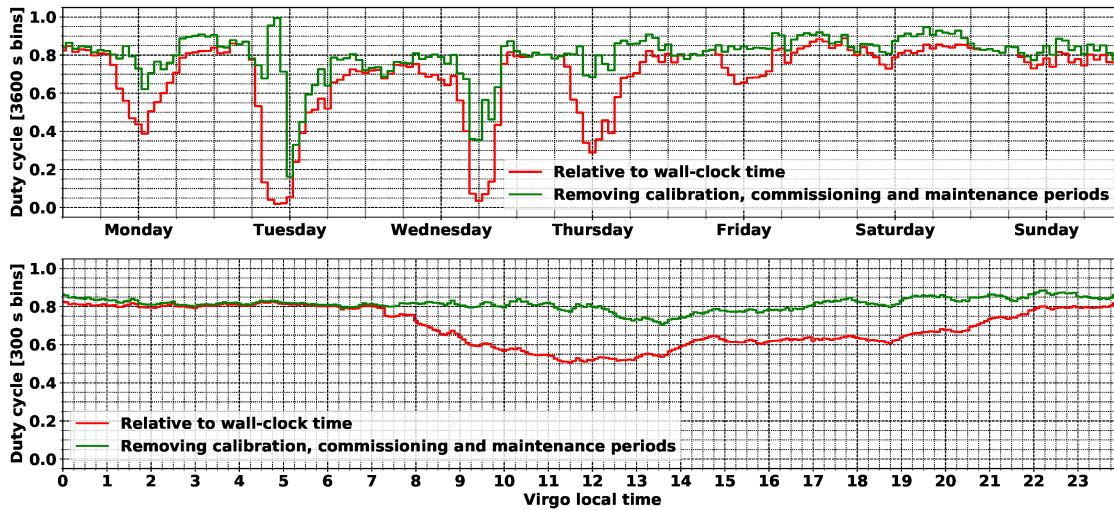


Figure 10: Average weekly (top) and daily (bottom) duty cycle of the Virgo detector during the O3 run. The red curve uses the elapsed real time as normalization, while the green one is produced excluding the times spent doing calibration, commissioning or maintenance, three activities that are incompatible with Science-mode data taking.

260 propagation speed up to a few km/s.

261 Since seismic waves excite buildings even at great distance, the Virgo monitoring set
 262 at EGO includes local, regional and teleseismic earthquakes since it was observed that
 263 all of them can induce large motion of the interferometer elements. This can then
 264 saturate the control capability of the feedback systems that keep Virgo at its nominal
 265 working point, leading to a loss of control. Following each control loss (regardless of
 266 its origin: an earthquake or another cause), data taking stops immediately and can
 267 only restart after the completion of the semi-automated sequence that allows restoring
 268 the Virgo global working point – during the O3 run, that procedure took about 20
 269 minutes on average [19]. But the time lost can be much longer in case of a control loss
 270 due to an earthquake, in case the suspension normal modes are excited by the seismic
 271 waves. In that case, one may have to wait up to one hour after the event that the
 272 high-quality factor modes of the suspensions are damped, before initiating the control
 273 acquisition procedure. Since each control loss reduces the Virgo duty cycle, it is therefore
 274 important to understand which fraction of these are due to earthquakes, and what are
 275 the earthquakes that induce them.

276 Large earthquakes at local and regional scale do not happen very often, so the type
 277 of earthquakes on which this analysis is focused is large earthquakes that occur along
 278 the boundaries of the main tectonic plates. Most of them are quite distant from EGO,
 279 meaning that a low-latency framework relying on data from a variety of seismic stations
 280 worldwide could produce early warning notices that would be received and processed
 281 *ahead* of the seismic waves arrival. In that case, one could take preventive measures to

282 try to mitigate the effect of the ground shaking, with the goal of avoiding the control
283 loss. In the following, we describe the strategy implemented at Virgo during the O3
284 run, that relies on the Seismon framework [28, 29, 30] developed at LIGO – an example
285 of the existing teamwork among members of the global GW detector network.

286 Furthermore, as explained below, the study has also highlighted another contribution
287 from much weaker earthquakes, quite close to EGO (the majority of which occur on the
288 Italian Apennines). Those have been more difficult to identify as they do not lead to
289 early warnings from Seismon and the frequency of their seismic waves is much higher
290 when they arrive at EGO: up to ~ 1 Hz, whereas teleseism waves are in the frequency
291 band 10 – 100 mHz. In addition, the proximity of their epicenters makes useless the
292 use of warnings that would always come too late. Thus, the only way to mitigate these
293 earthquakes is to understand how they impact the Virgo control system and what could
294 be done to strengthen it.

295 4.1. O3 Seismon setup at EGO

296 In addition to making the whole detector as robust as possible against the passing of
297 strong seismic waves, the only other leverage one can use to mitigate the impact of
298 earthquakes is to rely on early warnings provided by worldwide arrays of seismometers.

299 Following initial tests done during the O2 run and the upgrade period that followed, we
300 ran at EGO during O3 an instance of the Seismon framework, developed by LIGO to
301 process earthquake early warnings provided by the US Geological Survey (USGS) [31]
302 and to compute information relevant for each site of the LIGO-Virgo network. Namely,
303 for each earthquake, Seismon potentially predicts the arrival time of the different seismic
304 waves (P-, S- and surface), their amplitude at site and the probability of losing the
305 detector control in consequence of that earthquake. That framework was split into four
306 consecutive steps, each associated with a server integrated within the Virgo online data
307 acquisition system (DAQ) used to steer and monitor the detector.

- 308 • Reception of the USGS alerts.
- 309 • Processing of each alert by the Seismon framework.
- 310 • Extraction of the subset of Seismon data pertinent to the EGO site and provision
311 to the Virgo online framework.
- 312 • Local processing of these data.

313 In addition to producing a plot summarizing all information available from the early
314 warning, a loose cut is applied on magnitude and distance to estimate whether the
315 earthquake could be relevant, meaning that it could impact the control of the Virgo
316 detector. In that case, and if the warning was quick enough to precede the arrival of
317 the seismic wave on-site, an alarm would latch on the main panel of the Virgo Detector
318 Monitoring System [32, 33], alerting the operator on duty in the control room.

319 In the nominal O3 control configuration, the two 3 km-long optical cavities are kept in
320 resonance by acting on the end mirror suspensions: their actuators are the least noisy,
321 at the price of a reduced correction range availability. Actuators located at the level
322 of the input mirror suspensions have higher dynamics, while introducing slightly more
323 noise. Thus, they can be used as earthquake control mode (in short *EQ mode*) to try
324 to maintain the Virgo working point during periods of elevated seismic noise.

325 A smooth transition procedure, working both ways without losing the detector control,
326 has been developed to allow switching back and forth between end-mirror and input-
327 mirror actuations. During the O3 run, the procedure in use was the following: once
328 alerted by Seismon, the operator on duty would monitor the optics suspension status
329 and manually trigger the transition from nominal mode to EQ mode when the test mass
330 suspensions would start shaking significantly. Once activated, that process would take
331 a few tens of seconds to complete. Then, either the detector would nevertheless lose its
332 working point (and the control acquisition procedure would have to be restarted from
333 the beginning), or the EQ mode control would be kept until the whole seismic wave
334 trains has passed by and the suspensions motion has been damped back to levels low
335 enough to allow resuming the nominal control mode.

336 Unrelated to earthquakes, the EQ mode was also found useful during periods of high
337 wind: gusts shake the building structures (walls and floors) and those vibrations can
338 couple to the suspensions, potentially causing control corrections to saturate. However,
339 since EQ mode was not validated for the production of good quality data for physics
340 analysis, this method was used parsimoniously during most of O3 because corresponding
341 data would have to be discarded. A few weeks before the end of the run, the EQ mode
342 got finally qualified for regular data taking and later studies [34] showed that there was
343 no significant degradation of the Virgo sensitivity when switching to it. Therefore, it
344 was used more regularly from that time; the possibility to have such a backup solution
345 for O4 as well will be studied in the coming months.

346 4.2. Earthquakes impact during O3

347 The stronger and/or the closer to EGO the earthquake, the more likely it is to impact
348 the control of the Virgo detector. To study the impact of strong regional earthquakes
349 or teleseisms, the USGS warnings processed by Seismon are sufficient (as they should
350 include all such earthquakes). But it was soon realized that some moderate earthquakes
351 occurring at local and regional distance (from few tens to few hundreds kilometers away
352 from EGO), too weak to generate a USGS alert and thus not processed by Seismon,
353 could cause losses of control of Virgo. To check if any of the control losses was caused
354 by this type of earthquakes, we queried [35] the INGV (Istituto Nazionale di Geofisica
355 e Vulcanologia) public earthquake catalogue [36] to download the list of events that
356 occurred during O3 in the Mediterranean region. This list partly overlaps with the
357 USGS one and duplicates were removed. All results presented in the following are based

358 on the whole set of earthquakes, assembled by merging the USGS and INGV event lists.
 359 The control of the Virgo detector is extremely complex. Therefore, finding out how
 360 many earthquakes induced control losses during the O3 run required a careful study
 361 of all control losses, documented below in Appendix A. An earthquake from the list
 362 of USGS warnings is associated to a recorded control loss if the loss occurs within the
 363 time range during which seismic waves were predicted to arrive on-site according to
 364 Seismon and if the seismic activity around the time of the control loss is significantly
 365 larger than its typical range of variation. In case of concurring early warnings from
 366 different earthquakes overlapping in time at EGO, the strongest is arbitrarily selected
 367 as the reason for the control loss.

368 Estimating the strength of an earthquake when its seismic waves arrive at EGO is not
 369 easy. Yet, this is a key point to address, first to reject quickly warnings from harmless
 370 earthquakes and then to adjust the latency and level of response for the crew in charge
 371 of steering the Virgo detector. During O3, basic rectangular cuts in the magnitude-
 372 distance plane – e.g. *if magnitude > (...) or (distance < (...) km and magnitude >*
 373 *(...)) or etc.* – were applied to the live earthquake warnings received from USGS and
 374 processed by Seismon. During the post-run analysis, the ranking

$$\text{ranking} = \frac{10^{\text{magnitude}/2}}{\text{distance}[\text{km}]} \quad (1)$$

375 was introduced. While not complete – e.g. neither the hypocenter depth nor its azimuth
 376 angle computed with respect to EGO are accounted for – this ranking appears sound:
 377 the higher its value, the more likely the control loss. Applying a (conservative) minimum
 378 cut at ranking = 0.02 allows to safely remove more than half of the earthquakes to be
 379 analyzed.

380 Results shown below use the largest possible earthquake statistics, meaning that one
 381 requires the Virgo detector to be fully controlled, but not necessarily in Science mode.
 382 This looser requirement enlarges the dataset of interest and hence the number of
 383 earthquake early warnings to be taken into account.

384 Figure 11 highlights the epicentral distance and magnitude of the earthquakes that led
 385 to a Virgo control loss. The top (bottom) row deals with the earthquake magnitude
 386 (epicentral distance) while the right column displays the ratio of the red and blue
 387 histograms shown on the left column. As expected, the larger the earthquake magnitude,
 388 the more likely the control loss, with the fraction of earthquakes leading to a control
 389 loss departing from 0 for magnitude 6 and above. That fraction saturates to 1 (meaning
 390 that all events causes a control loss) when magnitude exceeds 7.2. We also note that
 391 the fraction is not null around magnitude 3: this reflects the control loss consequence of
 392 some small local earthquakes recognizable also in the left side histogram of Figure 11.
 393 The histogram ratio is much flatter for that other variable, with the most significant
 394 bins reflecting the location of seismic regions on the globe with respect to EGO, mainly

395 the broad Mediterranean area and the Ring of Fire (a region covering much of the rim
396 of the Pacific Ocean that is seismically very active).

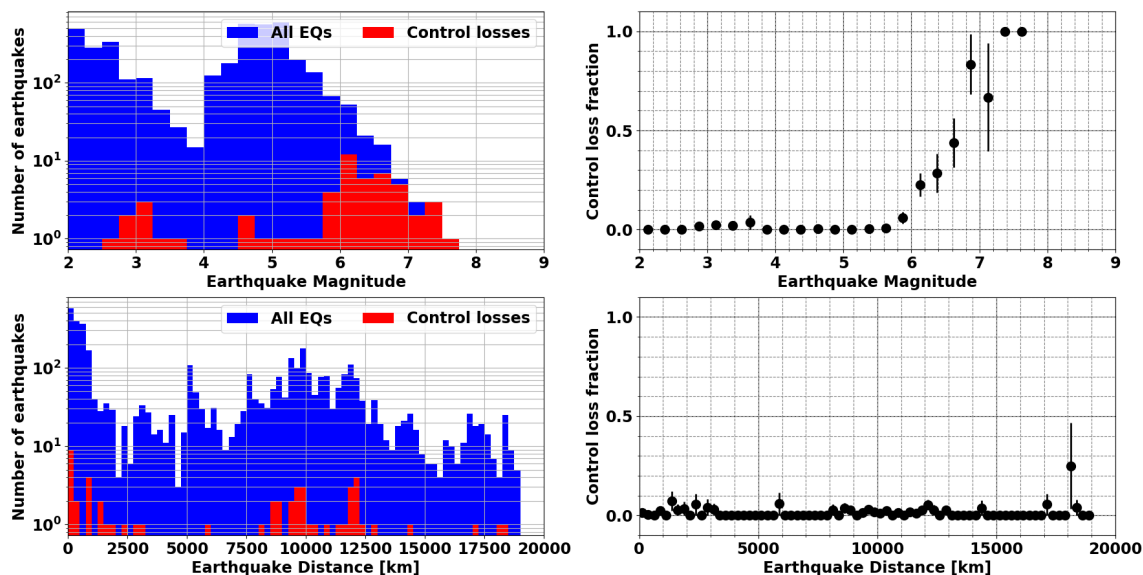


Figure 11: Summary of the impact of earthquakes on the Virgo detector during the O3 run. Left column: the blue (red) histogram shows all earthquakes (the earthquakes that have induced a control loss); top: magnitude distribution; bottom: distribution of the distance between EGO and the epicenter. Right column: corresponding fraction as a function of the earthquake magnitude (top) and distance (bottom). In all cases, the earthquakes that certainly could not impact Virgo (ranking below 0.02) were excluded.

397 Figure 12 shows the population of earthquakes that caused a control loss (red dots) in the
398 two-dimensional plane epicentral distance vs. magnitude. These earthquakes form the
399 upper envelope of the scatter plot drawn, meaning they are usually the earthquakes with
400 largest magnitude for any distance. The separation between red and green (earthquakes
401 that did not cause a control loss) dots is not perfect for at least two reasons. The first
402 one is that the control of the Virgo detector is complex enough that the actual level
403 of control (accuracy and stability) plays a role in whether or not the control is lost
404 for earthquakes at the limits of inducing a control loss. The second reason is that our
405 model could probably be improved by including other earthquake warning parameters:
406 two candidates would be the hypocenter depth (the deeper the hypocenter, the lower
407 the earthquake impact on the ground at equivalent magnitude) and the azimuthal
408 orientation of the epicenter with respect to EGO.

409 Figures 13 and 14 show the location of the significant earthquakes that occurred during
410 O3 with the same color coding used in Figure 12. Their distribution depicts the
411 boundaries of the main tectonic plates and, as discussed above, we can observe that the
412 most harmful earthquakes for Virgo are coming from the Mediterranean area (medium
413 to large magnitudes but smaller distances) and part of the Pacific Ring of Fire. The mid-

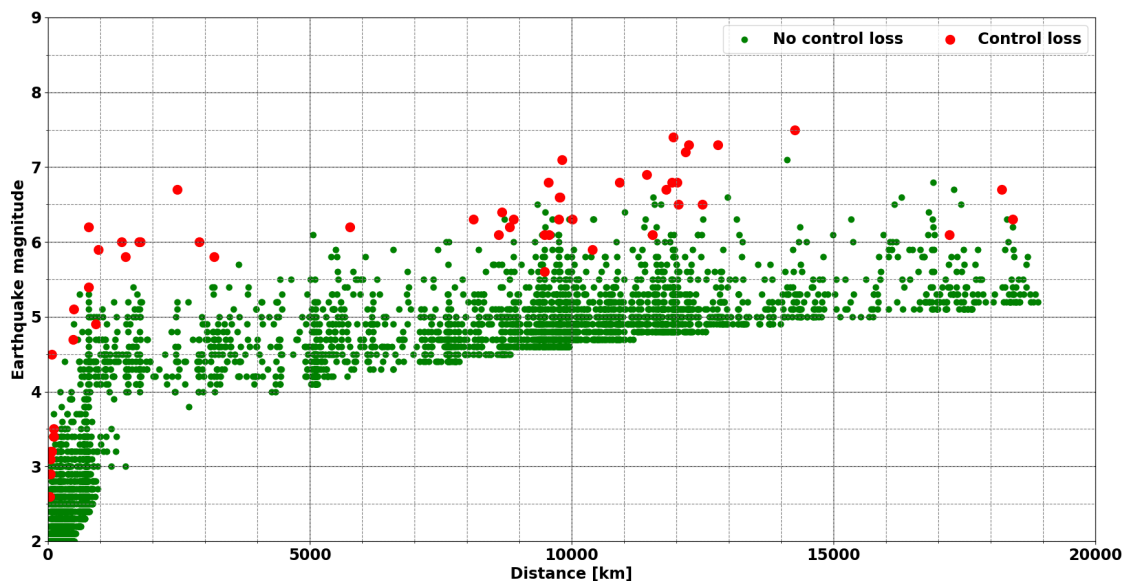


Figure 12: Distribution of earthquakes in the plane distance-magnitude during the O3 run. The earthquakes that caused a control loss (did not cause a control loss) are represented with red (green) dots. The lack of points below the main bulk of earthquakes is due to the ranking cut, set at 0.02.

414 Atlantic ridge and the Asian portion of the Alpidic earthquake belt did not produce many
 415 earthquakes that impacted Virgo, possibly because of the limited statistics. During the
 416 O3 run, the distribution of the earthquakes leading to control losses was the following:
 417 $\sim 15\%$ of close earthquakes; $\sim 20\%$ from other earthquakes in the Mediterranean area;
 418 and $\sim 65\%$ from distant earthquakes. We remark that this statistics has not an absolute
 419 meaning: the O3 run took place during a quiet seismic period for Italy, compared to
 420 e.g. 2009 or 2016. This analysis will be updated in the future with data from the O4
 421 run.

422 Finally, Fig. 15 shows an example of the impact of a strong and distant earthquake on
 423 the Virgo detector and how the early warning information was used to change the control
 424 mode prior to the arrival of the strongest seismic waves. This allowed the crew on duty to
 425 keep the working point of the instrument by preventing the correction force (applied on
 426 mirror suspensions to maintain resonance in the arm cavities) from saturating. Should
 427 that action not have been performed, the control loss would have been unavoidable – as
 428 the correction would have saturated around 22:27 UTC. The description of the different
 429 stripcharts displayed is given below.

- 430 • Top plot: variation of the index labelling the Virgo data taking configuration: the
 431 Science mode corresponds to the value 1; other indices shown here (-1, -7, -9)
 432 indicate different control configurations that are not nominal and that were used
 433 to wait for the right moment to switch back to Science data taking mode.

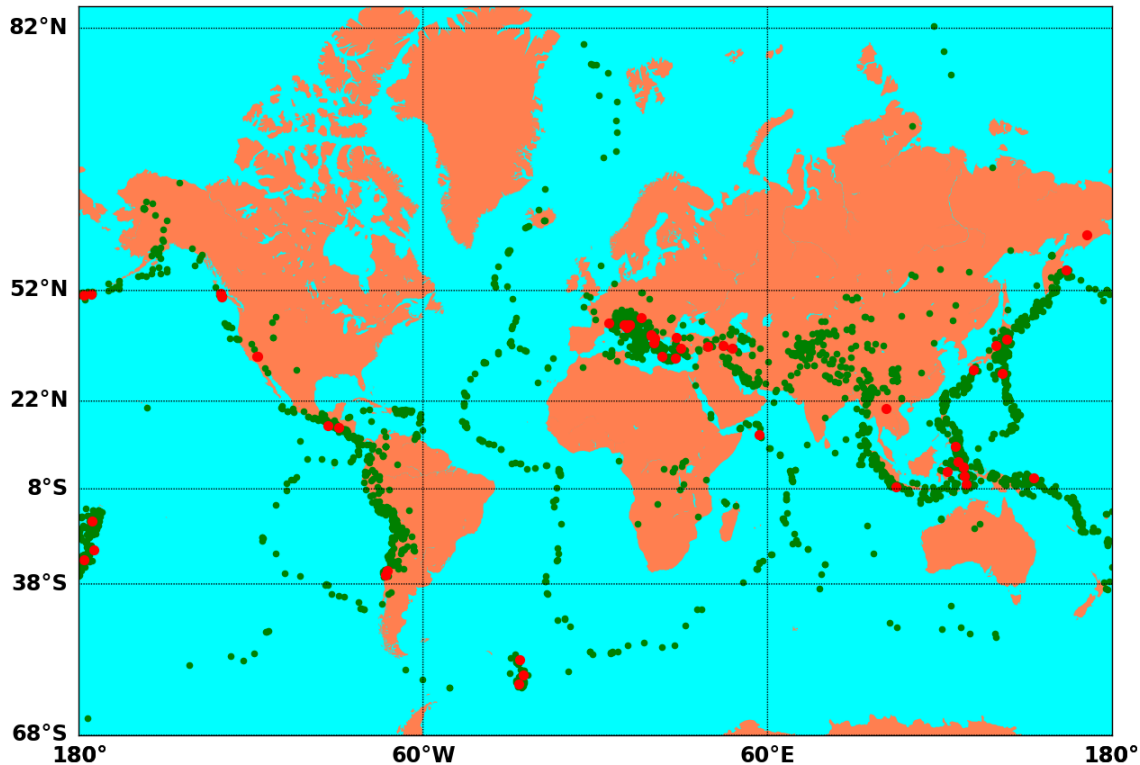


Figure 13: Location of the O3 earthquakes used in this study (ranking greater than 0.02) The earthquakes that caused a Virgo control loss (did not cause a control loss) are represented with red (green) dots.

- 434 • Second plot: stripchart of the BNS range versus time; the seismic waves clearly
 435 make the BNS range go down and fluctuate more while they are passing (see seismic
 436 activity variations recorded in the bottom plot, described below); the BNS range
 437 recovers its steady value at the end of the plotted time when the earthquake effect
 438 fades away.
- 439 • Third plot: switch showing the times when the earthquake-resilient control mode
 440 ('EQ-mode') is turned on ($0 \rightarrow 1$ transition) and later on off ($1 \rightarrow 0$ transition)
 441 manually by the operator on-duty.
- 442 • Fourth plot: For each second, maximum value of the correction applied on the test
 443 masses to keep the Virgo arms in resonance. When the nominal control mode is
 444 used, a control loss happens within two seconds at most after the time for which
 445 the correction voltage \S exceeds a 9.5 V threshold. This occurs a few times close to
 446 the middle of the time range represented here but no control loss follows, as the
 447 EQ-mode allows for larger corrections.
- 448 • Bottom plot: seismic noise measured in three orthogonal directions (vertical and

\S The mirror control is done by varying the amount of current applied to actuators (pairs of coil-magnet): see Ref. [17] for details.

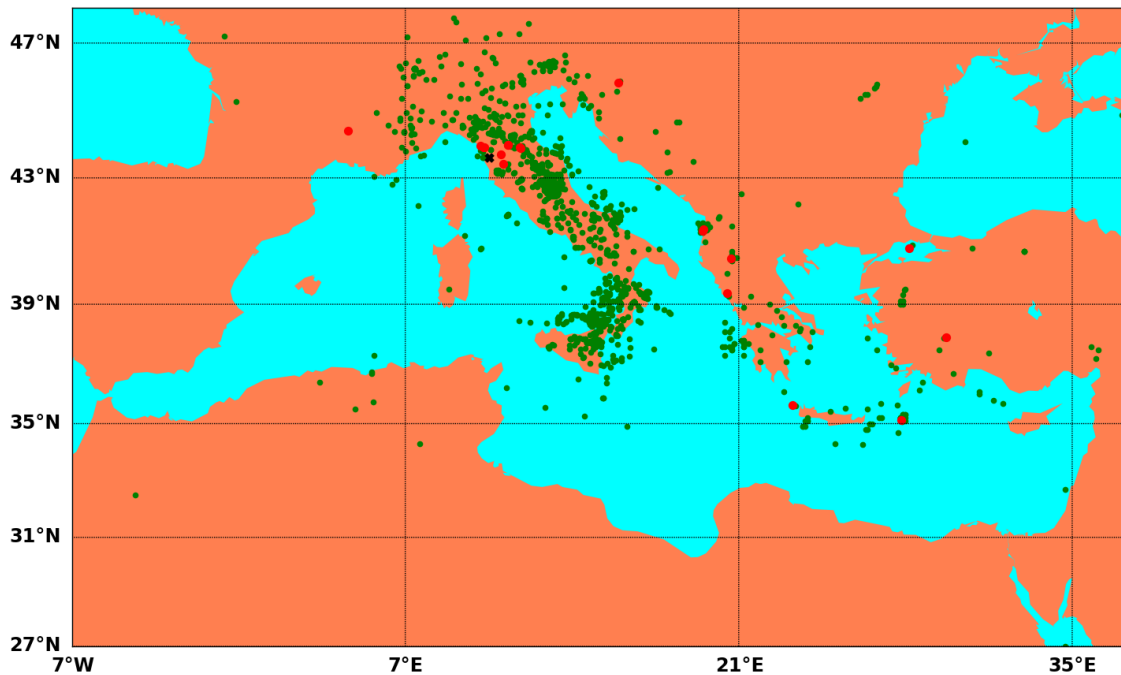


Figure 14: Zoom on the Mediterranean area of the map shown in Fig. 13 above. It shows the earthquakes nearby Virgo (whose site, EGO, is marked by a black cross) recorded during the O3 run. The earthquakes that caused a control loss (did not cause a control loss) are represented with red (green) dots.

449 along the two Virgo arms) using the dominant frequency range for earthquakes
 450 recorded at teleseismic distance: 10 mHz \rightarrow 100 mHz.

- 451 • Finally, the vertical dashed lines common to all plots show the time of important
 452 events. From left to right: the time at which the earthquake occurred; the time
 453 at which the corresponding USGS warning had been received and processed by the
 454 Seismon framework at EGO; the expected arrival time of the seismic P-waves, S-
 455 waves and Rayleigh waves. For the latter, we use three different arrival times that
 456 stem from different assumed velocities (5, 3.5 and 2 km/s respectively).

457 4.3. Plans for O4

458 Work is in progress to build on the O3 experience and have a more performing, better
 459 integrated, earthquake early warning framework for O4 (and beyond). The plan is
 460 to run the latest version of Seismon with an improved prediction capability for EGO,
 461 achieved by means of all the data collected during the O3 run. We are also exploring
 462 the possibility to use the INGV Early-Est system (a framework for rapid location and
 463 seismic/tsunamigenic characterization of earthquakes) [37, 38] as an additional source
 464 of warnings, complementary to USGS. Tests are in progress to have this new live stream

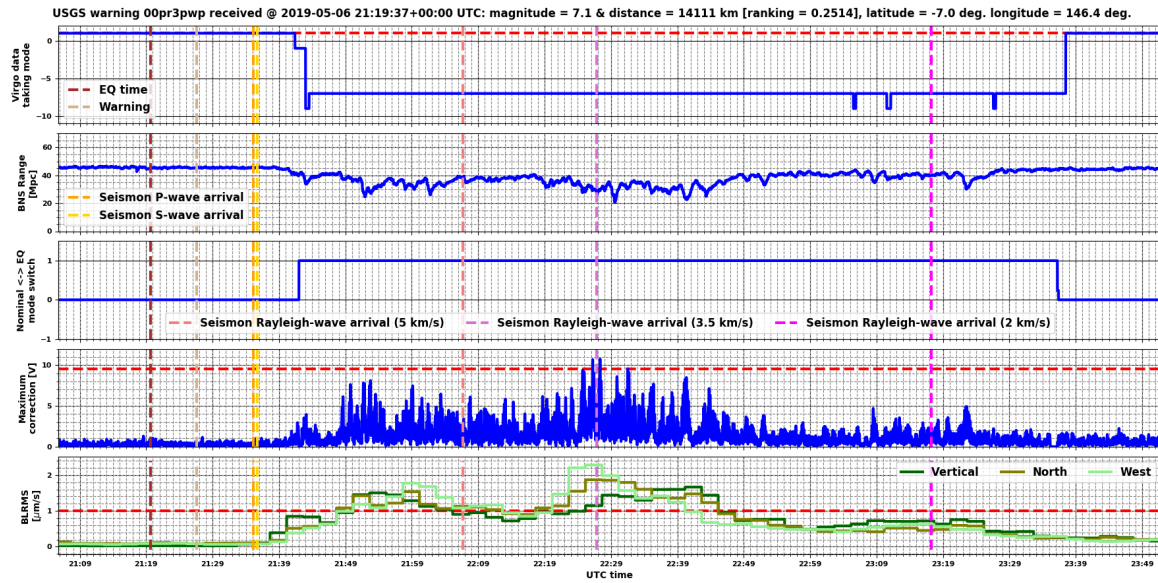


Figure 15: Example impact on the Virgo detector of a strong (magnitude greater than 7) and distant (14,000 km away from EGO) earthquake, that occurred on May 06, 2019 at 21:19:37 UTC in Eastern Papua New Guinea. The description of the different stripcharts is provided in the text.

465 received at EGO and integrated into the existing framework. The two sets of early
 466 warnings will then be compared, in terms of latency and accuracy.

467 5. Bad weather

468 Through O3, the Virgo interferometer performed worst during days with adverse
 469 meteorological conditions, namely high winds and intense sea activity. These periods
 470 were generally associated with increased non-stationary noise in the GW signal below
 471 about 100 Hz and with some difficulties in maintaining the interferometer in its
 472 controlled state, resulting in reduced duty cycle. In the following, we study the impact
 473 of the increased microseismic noise associated to sea waves, then the influences of wind
 474 on BNS range, as well as the effect of wind gusts on the global interferometer controls.
 475 Because of the wind action on the sea surface, high winds and rough sea often occur
 476 together. We use a statistical approach to disentangle their effects on the detector.

477 5.1. Impact of sea activity

478 Microseism amplitude at EGO increases by more than one order of magnitude between
 479 calm and rough sea periods. For 10% of the time during O3, ground RMS velocity
 480 between 0.1 Hz and 1 Hz was above 4 $\mu\text{m/s}$, as shown in Fig. 5. This happened in
 481 particular in correspondence of the seasonal change in the first part of O3b and for

482 some periods of adverse weather conditions in the first months of 2020. Periods of
 483 intense sea activity were associated to larger than usual strain residual noise whose
 484 characteristics and origin require further analysis.

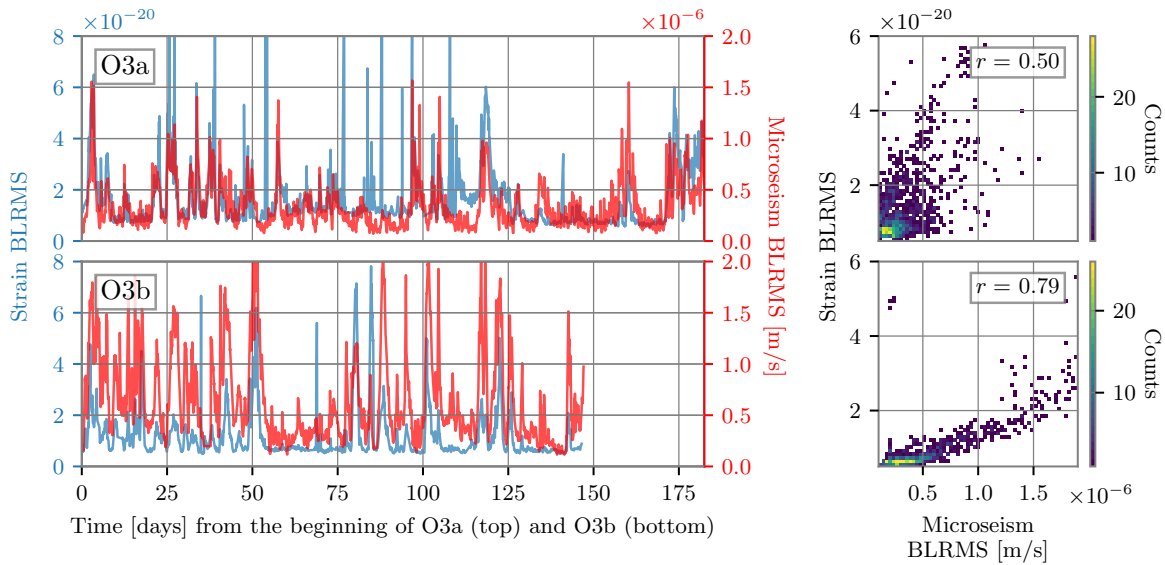


Figure 16: Correlation between the low frequency noise in Virgo GW strain and the microseism induced by the sea activity; top row for O3a and bottom for O3b. Left: in blue the time series of the strain BLRMS in band $[10, 20]$ Hz and in red that of the BLRMS in band $[0.1, 1]$ Hz of a CEB seismometer, mostly influenced by the sea activity. Right: 2D-histograms of the correlation between the two BLRMS, where the colorscale counts, for every pixel in this map, how many data points have the corresponding values of strain and microseism BLRMS. The annotation in the top-left corner reports the value of the Pearson correlation coefficient r .

5.1.1. *Microseism impact on strain noise* Periods of high sea activity were associated with larger strain residual noise up to about 100 Hz. To characterize this effect, we made use of the *band-limited* RMS (BLRMS), defined for a generic signal, in a certain frequency band $[f_{\min}, f_{\max}]$, as:

$$\text{BLRMS}(t; [f_{\min}, f_{\max}]) := \sqrt{\int_{f_{\min}}^{f_{\max}} S(f; t) df} \quad (2)$$

485 where $S(f; t)$ is an estimate of the signal *power spectral density* (PSD) referred to a time
 486 t .

487 In Fig. 16, we report, for the entire O3 run, in blue the BLRMS of the strain in the band
 488 $[10, 20]$ Hz and, in red, the CEB seismometer BLRMS in the band $[0.1, 1]$ Hz. These have
 489 been estimated from (2), where $S(f; t)$ is computed with the Welch's method making

490 use of strides of 2048 seconds and FFT length of 128 seconds, overlapping by 50% [39].
 491 The correlation between the two curves is apparent. In particular, when the microseism
 492 is intense, the peaks in the strain BLRMS are almost everywhere coincident with those
 493 in the seismometer BLRMS. This fact is also highlighted in the 2D-histograms on the
 494 right-hand side of the same figure, where the Pearson correlation coefficient has been
 495 computed for the two data taking periods, O3a (top) and O3b (bottom). In general,
 496 we observe that, despite the “spikes” in correspondence of bad weather conditions (in
 497 particular at the beginning of O3b and then during most of Winter||), the induced strain
 498 noise at low frequency has improved during O3 and can now be mostly attributed to
 499 microseism.

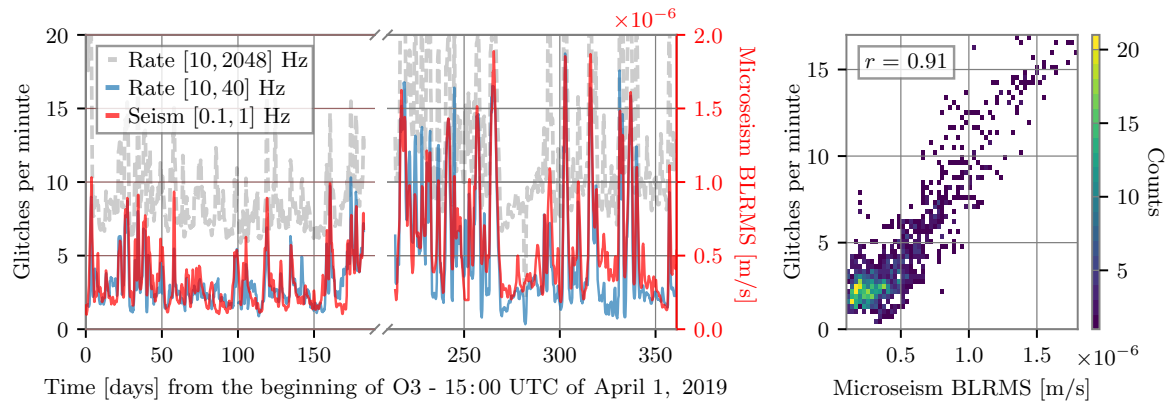


Figure 17: Correlation between Virgo glitch rate and the sea induced microseism during the O3 run. Left: the dashed gray line represents the daily moving median of the glitch rate per minute recorded by Omicron [40] for glitches with SNR > 6.5 and frequency at peak in band $[10, 2048]$ Hz, estimated over strides of 2048 seconds. The blue continuous line is the median rate referred to glitches with frequency at peak in $[10, 40]$ Hz band. The continuous red line is the BLRMS in band $[0.1, 1]$ Hz of a seismometer in the Virgo CEB. Right: 2D-histogram of the glitch rate in band $[10, 40]$ Hz and the microseism BLRMS, where the colorscale counts, for every pixel in this map, how many data points have the corresponding values of the rate and the microseism BLRMS. The annotations in the top-right corners report the values of their Pearson correlation coefficient r .

500 *5.1.2. Microseism impact on glitch rates* Besides an increase in the RMS value of the
 501 strain noise at low frequency, microseisms induce short transients of power excess in
 502 this channel, colloquially referred to as *glitches*. In Fig. 17 we report the minute rate of
 503 these glitches during the entire O3 run. To reduce the – usually very large – variability
 504 in their rate, we computed running daily medians. The gray dashed line represents the
 505 time evolution of daily medians for glitches with SNR > 6.5 and frequency at peak in

|| That calendar season starts around day 50 of O3b and lasts almost until the end of the data taking.

506 the band [10, 2048] Hz, as measured by the online Omicron pipeline [40]. The blue solid
 507 line is the median minute rate of glitches with peak frequency in the [10, 40] Hz band.
 508 These glitches accounted for about 30% of the total during O3a, and for almost 40% in
 509 O3b, with peaks larger than 80% in correspondence of periods of intense sea activity.
 510 This glitch rate is highly correlated with microseism, represented in the left-hand side
 511 plot of Fig. 17 by the solid red line of the running weekly median of the BLRMS in
 512 band [0.1, 1] Hz of the CEB seismometer. On the right-hand side of the same figure, we
 513 report the 2D-histogram of these two quantities and the value of their Pearson coefficient
 514 ($r = 0.91$).

515 *5.1.3. Microseism and scattered light* Glitches due to microseism often resemble arches
 516 in a time-frequency map, as illustrated for example in Fig. 18. Arches are the typical
 517 signature of scattered light (SL) noise processes, which is a major issue and topic of
 518 investigation in the second generation GW detectors [12, 13, 14, 41, 42, 43].

519 A stray light beam bouncing off a moving surface adds coherently to the beam main
 520 mode every time its optical path, $x(t)$, changes (increases or decreases) by an integer
 521 wavelength. It follows that the frequency of the strain noise is:

$$f_{sc}(t) = \frac{2n|\dot{x}(t)|}{\lambda} \quad (3)$$

522 where $\dot{x}(t)$ is the instantaneous relative velocity between the interferometer beam and
 523 the scatterer, and $\lambda = 1.064 \mu\text{m}$ is the Virgo laser wavelength. Equation 3 is referred
 524 to as predictor. In case the scattered beam encounters a second reflective surface it can
 525 bounce back and forth n times along the same path before recombining, giving rise to
 526 higher order noise arches, reaching out n -times larger frequencies.

527 In O3 the main sources of scattered light affecting the sensitivity were the suspended
 528 optical benches placed beyond the end test masses in the terminal buildings (SNEB,
 529 SWEB). In this case, the noise observed in the time-frequency domain is well visible as
 530 power fluctuations in the cavity. The noise appears as a series of arches, where the typical
 531 non-stationarity and non-linearity of the noise is evident. Arch time spacing is the half-
 532 period of the oscillation of the mirror-bench relative motion, and arch amplitude (i.e.
 533 the maximum frequency extension of the induced strain noise) is $f_{max} = (4\pi/\lambda)AFn$
 534 where A and F are the amplitude and frequency of the oscillation. If the frequency
 535 and amplitude of the oscillation are such that $f_{max} > 10$ Hz, the noise affects the GW
 536 detection frequency band.

537 Being those benches suspended and controlled [44], their motion induced by the
 538 microseism was supposed to be attenuated enough to push the maximum frequency of
 539 the arches below 10 Hz. Moreover, a control technique taking into account the mirror-
 540 bench differential signals was implemented in order to reduce their relative motion
 541 (BENCH-MIRROR), which is the quantity effectively responsible of the noise coupling.

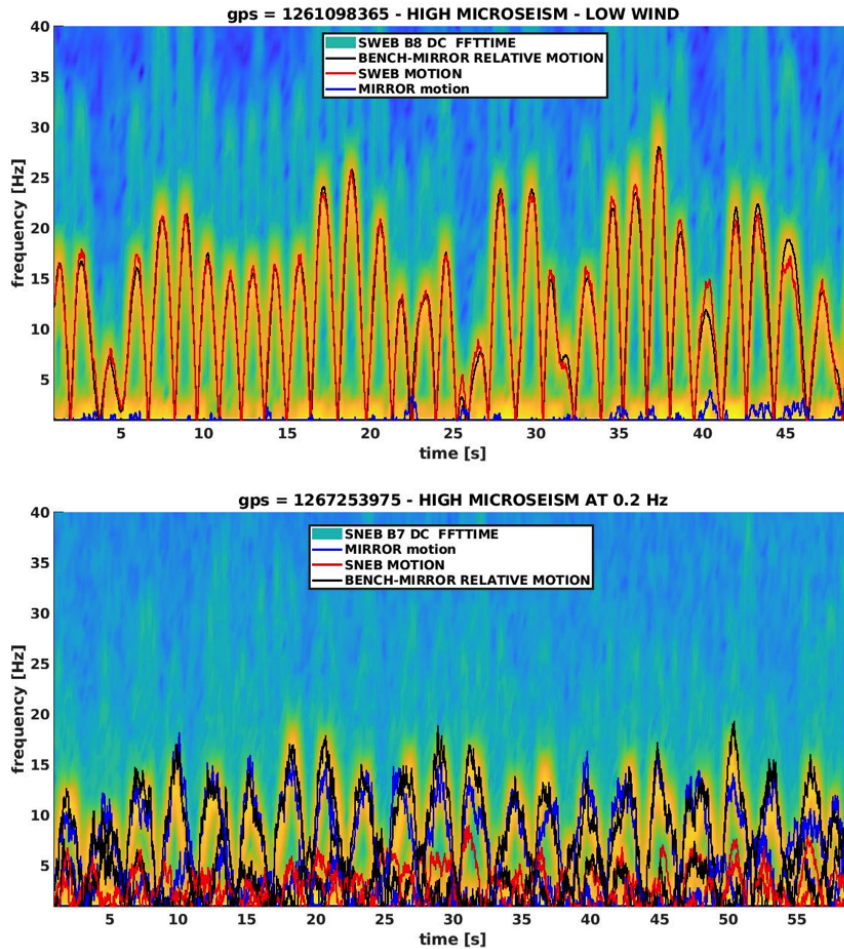


Figure 18: Spectrograms of the light transmitted at the end of the arm cavities and detected by photodiodes located behind, on suspended benches – top plot: west arm, B8 photodiode, SWEB bench; bottom plot: north arm, B7 photodiode, SNEB bench. The typical pattern of scattered light noise (arches) – both first order and second order (higher frequencies) – is visible. On the SWEB plot, arch spacing and amplitude correspond to half the period of marine microseism at Virgo (~ 3 s) and a ground velocity of about $8 \mu\text{m/s}$. The predictor for BENCH-MIRROR is shown in black, while the predictors computed from mirror and bench motions are shown in blue and red, respectively. The overlap shows that BENCH-MIRROR is the best predictor of scattered light, closely matching the observed arches.

542 During O3, a malfunctioning was identified in the mechanical setting of the West
 543 Bench suspension (SWEB) which caused its actual motion to be comparable to the
 544 ground motion at the frequency of the main microseismic peak. Figure 18 shows the
 545 mirror contribution and the bench contribution to the arches separately, for both North
 546 and West cavity, in two selected bad-weather conditions. In the West arm power
 547 spectrogram, the typical pattern is visible: the arches were entirely due to SWEB
 548 motion, and all the times the ground motion exceeded a certain threshold during the

run, these arches entered the detector band. In the North arm power spectrogram, the arches were normally much lower, and the contribution from the bench motion was of the same magnitude as the mirror motion. It was even possible to find some special conditions (the largest component of the ground motion centered at 0.2 Hz), in which the mirror motion was prevalent (see Figure 18, bottom panel).

The issue concerning SWEB mechanics and control has been understood and cured after O3. In O4, its residual motion is expected to be at least similar to the one observed in O3 for SNEB. Further improvements in the control strategy will be tested for both the mirror and the bench suspension.

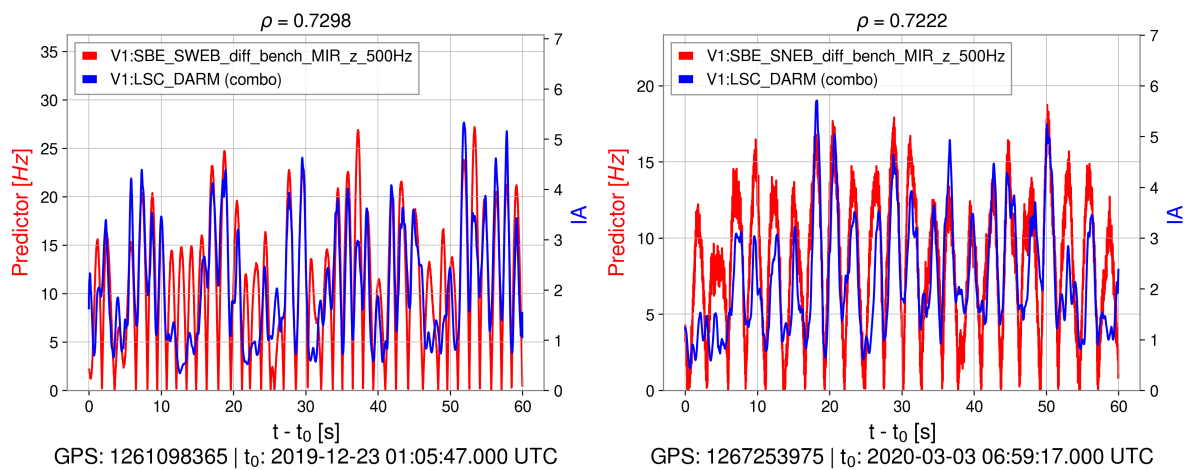


Figure 19: In red is the culprit’s predictor, i.e. Equation 3 for the relative motion (diff) between the suspended end bench and the end mirror (BENCH-MIRROR) of the West end (left) and North end (right). The sum of the IA of the first two modes of DARM, extracted by tvf-EMD is shown in blue.

5.1.4. *Identification of scattered light culprits* Part of the effort regarding scattered light noise mitigation consists in the localisation of scattered light sources, referred to as culprit, through data analysis. This can be a difficult and time consuming operation in a km-long detector with many possible sources of SL. Adaptive algorithms for time series analysis can be used to this end, due to their ability to decompose non-linear and non-stationary data into a set of oscillatory modes [45, 46]. The methodology described in [46] and based on the time varying filter empirical mode decomposition (tvf-EMD) [47] adaptive algorithm is applied to the two data segments shown in Fig. 18. SL noise couples with the differential motion of the arm cavities (*DARM*, the Virgo longitudinal degree of freedom sensitive to GW) time series, which is first low-passed and then decomposed using tvf-EMD to extract its oscillatory modes, from which the instantaneous amplitude (IA) is obtained using the Hilbert transform. Computing Equation 3 for a broad list of position sensors and correlating with the IA of *DARM*’s

571 oscillatory modes allows to quickly identify the most correlated channel, i.e. the culprit.
 572 The two data segment considered are

- 573 • GPS: 1261098365 UTC - 2019/12/23 01:05:47 + 60s,
- 574 • GPS: 1267253975 UTC - 2020/03/03 06:59:17 + 60s.

575 Obtained results are reported in Fig. 19, showing the predictors of the culprit for the end
 576 benches, based on Equation 3, correlated with the IA of DARM. The culprits are related
 577 to the BENCH-MIRROR channel in both cases. The resulting values of correlation are
 578 $\rho = 0.73$ for SWEB and $\rho = 0.72$ for SNEB. Since after low-passing the data the first
 579 two oscillatory modes of DARM were found to be the most correlated with the same
 580 predictor, the sum of their IA is considered and is shown in Fig. 19 for both cases,
 581 referred to as *combo*. As a counter proof, in Fig. 18 the predictors of the culprits are
 582 overlapped on the spectrograms of the WEB and NEB photodiodes. It can be seen
 583 that they closely match the scattered light arches. In particular, for the SWEB case,
 584 the mirror motion is small and the bench motion is mainly responsible for the observed
 585 scattered light. For SNEB case, while the mirror motion is significant the BENCH-
 586 MIRROR predictor, identified with adaptive analysis, better matches the arches also in
 587 this case.

588 5.2. Impact of wind

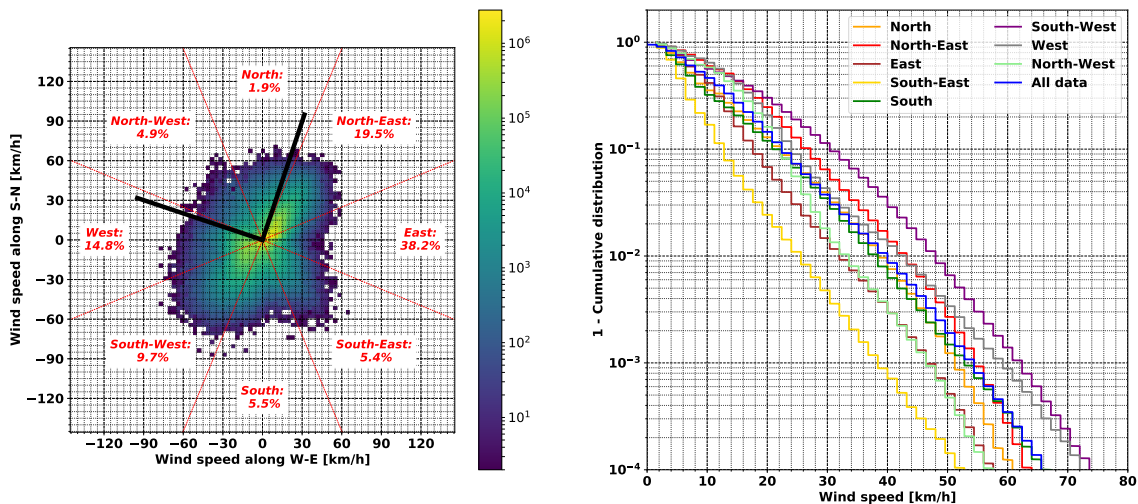


Figure 20: Wind statistics as measured by the EGO weather station during the O3 run. The left plot shows the joint distribution of the wind speed and orientation, with the two black bars showing the directions of the two arms of the Virgo detector. The right plot shows the complementary cumulative distribution of the wind speed for each of the eight quadrants of the wind rose.

589 Figure 20 summarizes the wind statistics recorded at EGO during the O3 run. Wind is
 590 blowing more often from the East while the stronger winds are predominantly coming
 591 from the West – the sea shore. The method described in Sec. 3.2.1 can be applied to
 592 quantify the impact of the instantaneous wind speed on the sensitivity. Figure 21 shows
 593 that the sensitivity is pretty much unaffected until a wind speed of $\sim 20 - 25$ km/h,
 594 while the detector gets sensitive to larger speeds: the BNS range decrease exceeds
 595 ~ 4 Mpc for a wind speed of 50 km/h or above. Yet this variation is limited (about
 596 10% of nominal BNS range values during O3), meaning that the detector is quite robust
 597 against wind. Another consequence of high-wind conditions is the need for the Virgo
 598 global control system to use larger corrections to keep the instrument at its nominal
 599 working point. And the larger these corrections, the more the detector is vulnerable to
 600 additional disturbances that could make the corrections saturate and lead to an almost
 601 immediate control loss.

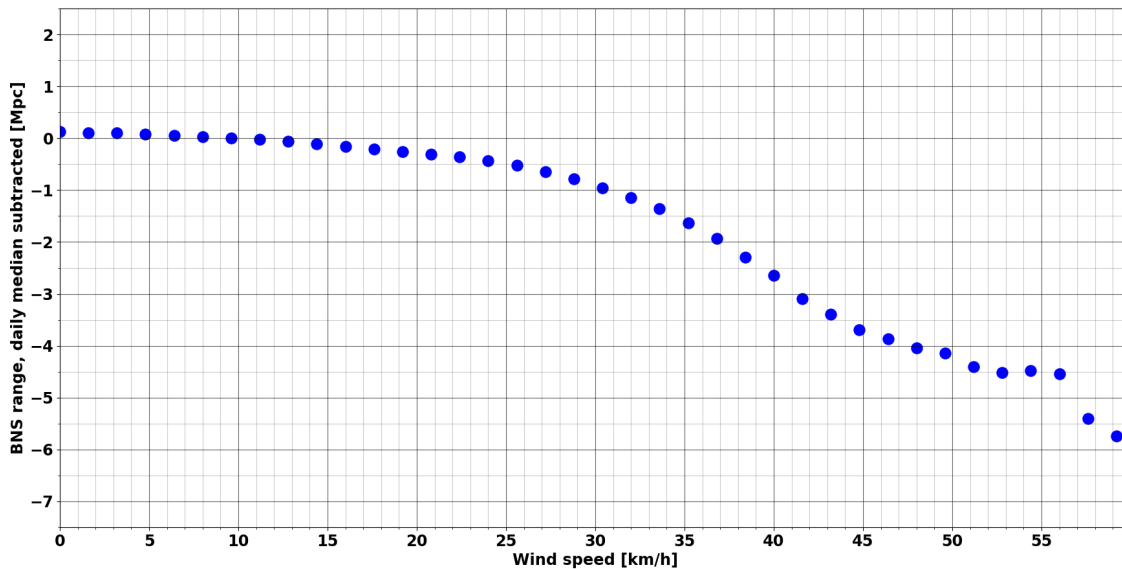


Figure 21: Average variation of the BNS range around its local average, as a function of the wind speed. In the Virgo DAQ, the BNS range and the wind speed are updated every 4 and 2 seconds, respectively.

602 The effect of the wind speed is clearly visible on Fig. 22 that compares the
 603 complementary cumulative distribution functions of the kilometric Fabry-Perot cavity
 604 longitudinal corrections for different ranges of wind speed. Clearly, the larger the wind
 605 speed, the higher the correction. On this plot, the average wind speed and the maximum
 606 correction have been computed using non-overlapping time windows of 30 seconds each.
 607 The largest displayed correction range stops on purpose at 9 V because the actual
 608 physical correction saturates at 9.5 V, a value that can be reached or even exceeded
 609 when there is a control loss. As the control system has some small but non-zero internal
 610 latency, it is not always clear whether the observed saturation is the cause of the control

611 loss or a consequence of it. Therefore, for a cumulative plot like the one shown on Fig. 22,
 612 corrections above 9 V have been cut away to avoid contamination from correction signals
 613 posterior to control losses.

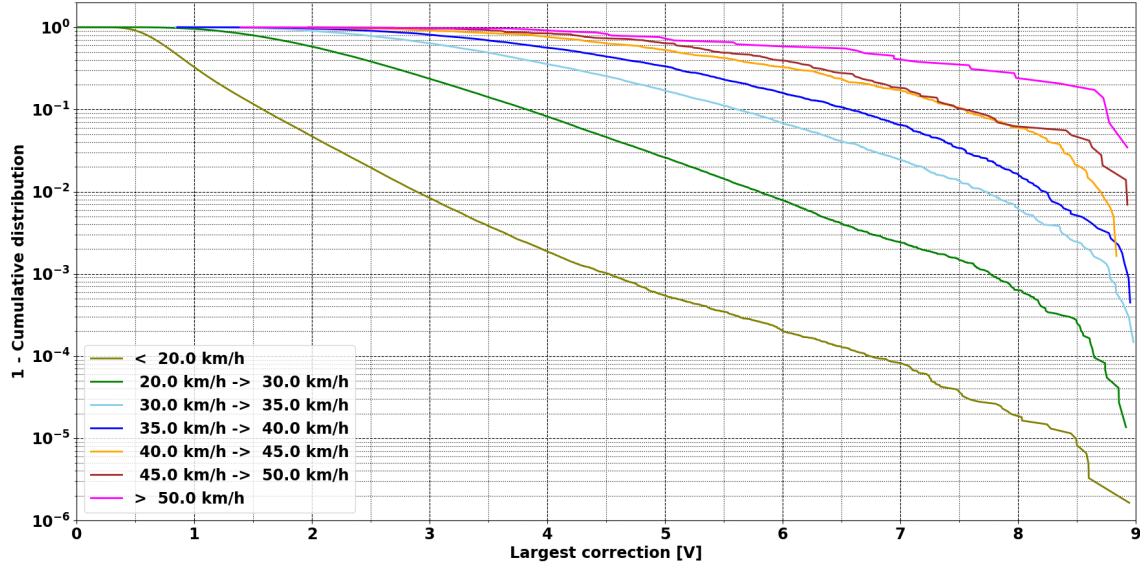


Figure 22: O3 complementary cumulative distribution functions of the maximum longitudinal corrections (in volts) keeping the Virgo arm cavities resonant for different wind speed ranges. The mean wind speed and the maximal corrections have been computed over 30 s time windows. The x -axis ends at 9 V, a bit below the saturation level of 9.5 V for that particular correction.

614 5.3. Disentangling sea activity and wind

615 Fig. 23 attempts to disentangle the impact of high microseism levels (due to the nearby
 616 rough sea) and high wind, by looking at the O3 Virgo duty cycle as a function of
 617 the microseism level for three different wind conditions: no cut on wind speed (blue
 618 histogram); low wind speed (below 25 km/h, green); high wind speed (above 25 km/h,
 619 red). One can see that in low wind conditions the duty cycle is pretty much independent
 620 from microseismicity, whereas it is lower and decreases more quickly when the wind level
 621 increases. Therefore, the Virgo detector appears robust against microseism but more
 622 sensitive to wind. Note that the extreme bins on the histograms plotted on Fig. 23 may
 623 have low statistics compared to others (low wind and high microseism, or high wind and
 624 low microseism are rare conditions): this explains why the duty cycles reported there
 625 fluctuate significantly compared to neighboring bins.

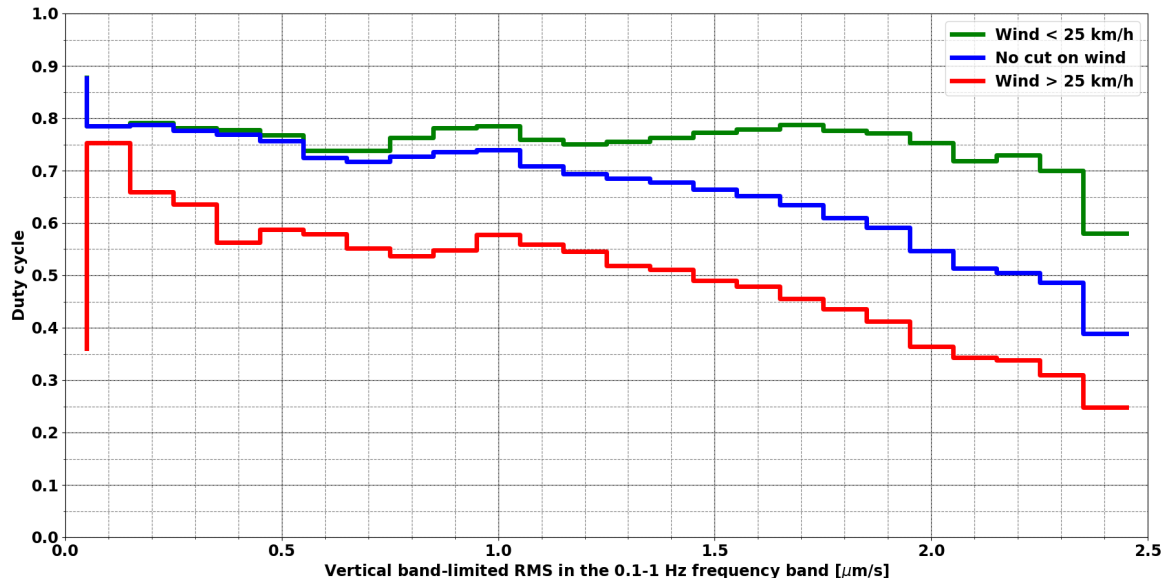


Figure 23: Virgo duty cycle during the O3 run versus microseism activity, for three different wind conditions: blue \leftrightarrow no cut on wind speed; green \leftrightarrow low wind (speed below 25 km/h); red \leftrightarrow high wind (speed above 25 km/h).

6. Other environment impacts

Additional sources of external noise have potential impact on the interferometer. Hereafter we describe those sources that we have further investigated during O3, namely: Schumann’s resonance magnetic fields, lightning strikes and cosmic ray muons.

6.1. Magnetic noise

Ambient magnetic fields can couple to GW interferometers, for example through the magnetic actuators used for the control of the seismic isolation platforms of optical components and of the test masses [12, 48]. Like gravitational waves, electromagnetic (EM) waves travel at the speed of light, and, due to their strength, could affect multiple detectors with time differences compatible with those expected from some GW.

Magnetic fields that extend over the entire planet, such as the Schumann resonances [49] (SR), or large-current lightning strikes, can limit the sensitivity to GW signals correlated over multiple detectors [50, 51]. One purpose of the EGO external magnetometers (see Sec. 2) is to monitor the level of these global magnetic fields.

At Virgo, the external magnetic environment is much quieter than inside experimental halls where stray magnetic fields are radiated by electric loads and cables where large currents are circulating. Figure 24 compares inside and outside magnetometer spectra recorded at Virgo during O3 and in the very quiet environment inside the Sos Enattos mine in Sardinia [52]. The most intense spectral noise features are narrow lines at the

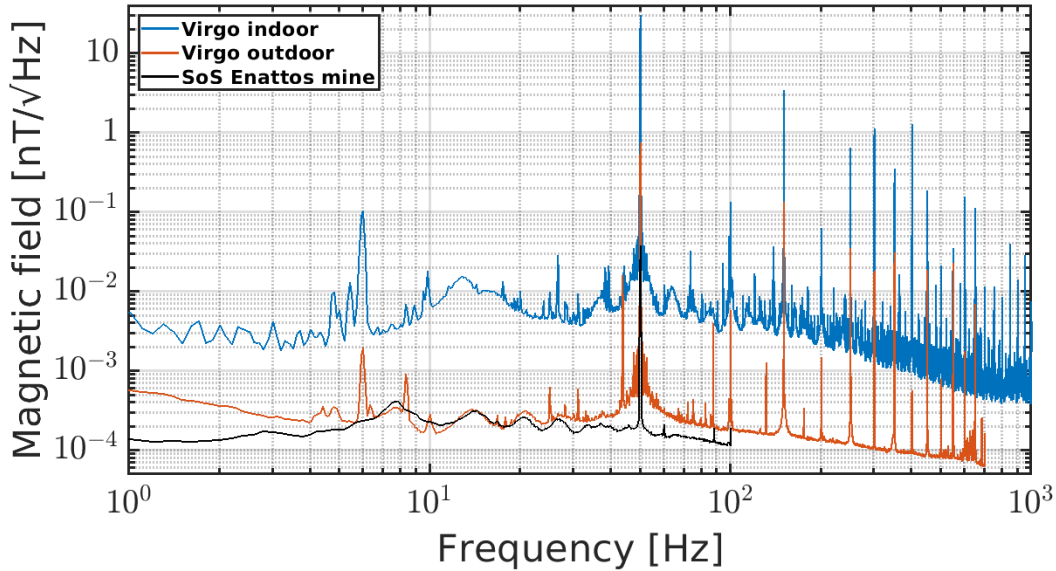


Figure 24: Amplitude spectral densities of indoor (blue curve) and outdoor (red curve) magnetometers at EGO and at Sos Enattos mine in Sardinia (black curve). The quiet Sos Enattos location shows evidence of Schumann resonances peaked at approximately 8, 14, 21, 27 and 33 Hz.

645 50 Hz electric mains frequency and its odd harmonics. The RMS amplitude of the 50 Hz
 646 line measured at Virgo is of the order of 0.1 nT in the external location, while it is at
 647 least 50 times larger in any inside location.

648 Virgo external magnetometers detect the SR field. This consists of steady EM waves
 649 that resonate inside the waveguide formed by the Earth surface and the ionosphere, and
 650 which are excited by globe-wide lightning activity. The second and third SR modes
 651 (peak frequency around 14 Hz and 21 Hz, respectively) are visible above noise at almost
 652 any time, their median amplitude during O3 is a few tenth of pT, their intensity follows
 653 a 24-hour modulation. The measured daily modulation of the third SR mode is shown
 654 in Fig. 25. This modulation is thought to be associated to temperature-driven variations
 655 in the height of the ionosphere EM waveguide [53]. The first SR mode and those of order
 656 greater than three, are often covered by anthropogenic magnetic noise. Figure 25 shows
 657 that during the COVID-19 lockdown period from March to May 2020, the external
 658 magnetic field median RMS in the low frequency region from 1 to 6 Hz reduced by
 659 about 50% with respect to the reference period between December 2019 and February
 660 2020. At the same time, the magnetic field RMS amplitude between 18 Hz and 24 Hz
 661 around the 3rd Schumann mode, did not change appreciably.

662 At EGO, anthropogenic external magnetic noise follows a daily modulation: broad
 663 maxima during working hours and minima around 01:00 LT. This noise has the form
 664 of short transients with intensity of ≈ 10 pT extending from DC up to approximately
 665 20 Hz. We believe this noise is associated to train transits along railway tracks at about

666 6 km distance from the site. The sudden trunk-line change when a train passes from an
 667 electro-duct section to another one creates stray currents and magnetic fields that are
 668 observed as magnetic glitches at EGO. According to the measured coupling of ambient
 669 fields [12] we estimate a negligible impact of Schumann's and anthropogenic magnetic
 670 noise on the sensitivity of the future Virgo upgrades. More relevant might be the impact
 671 of the correlated Schumann noise on multiple interferometers, which is under evaluation.

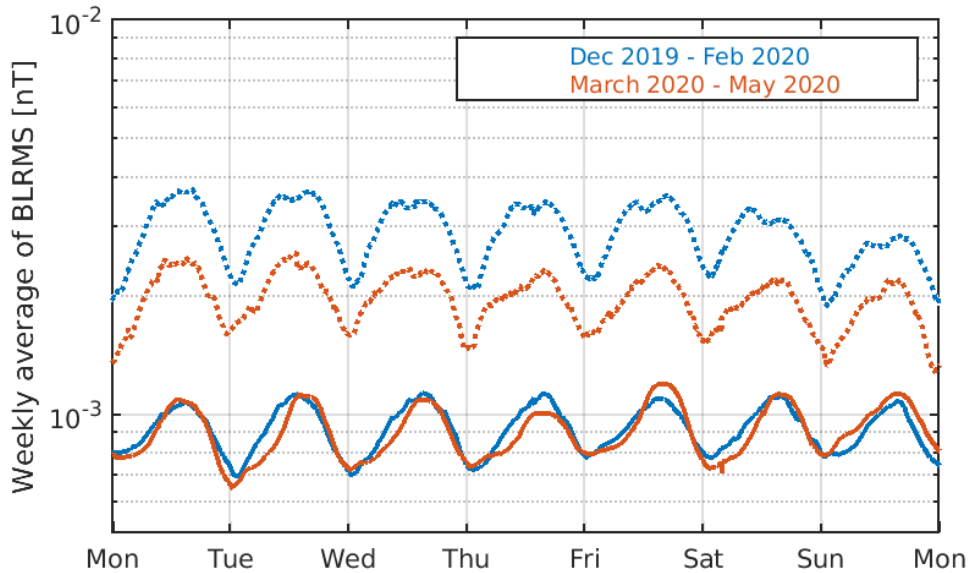


Figure 25: Weekly averaged magnetic field band-limited RMS values computed in two frequency bands: 1 to 6 Hz (dashed) and 18 to 24 Hz (solid). Magnetic field intensity is measured externally of Virgo experimental buildings, in the reference period between December 2019 and February 2020 (blue curves) and in the period between March 15 and May 15 (red curves) which corresponds to reduced anthropogenic activity within and outside of EGO because of the COVID-19 pandemics.

672 6.2. Lightnings

673 Lightning strikes produce prompt EM waves and much slower air pressure waves which
 674 induce vibrations of the ground and of the detector mechanical components. There are
 675 studies of correlated lightnings noise between the Virgo and LIGO sites [51] and at the
 676 KAGRA underground observatory [54].

677 The typical effect of the impact of a lightning strike occurring at approximately 10
 678 kilometers from the Virgo detector during O3 is illustrated in Fig. 26. A distinctive
 679 feature of lightning strikes is a coincident short transient noise in magnetometers located
 680 inside the 3 km-distant Virgo experimental buildings (top graph of Fig. 26). The
 681 magnetic impulse is followed by the slower sound shock wave detected by seismometers

682 (middle graph of Fig. 26). The bulk of displacement noise reaching the buildings is
 683 below 10 Hz.

684 The bottom graph of Fig. 26 illustrates the effect of the lightning in the GW strain signal.
 685 In coincidence with the spike in magnetometers, we observe a prompt broadband low-
 686 frequency noise and the onset of a 48 Hz narrow spectral noise, with a minute-long decay
 687 time, leading to a $\sim 30\%$ drop of the live BNS range. This latter noise has been associated
 688 to one structural mode of the West end test mass suspension, which gets excited because
 689 of the coupling of ambient magnetic fields with the magnetic actuators located along
 690 the suspension. Moreover, associated with the delayed acoustic and seismic bursts of
 691 ambient noise reaching the experimental buildings, a broadband strain noise shows up,
 692 extending up to about 100 Hz. This is likely due to scattered light processes within the
 693 interferometer.

694 Data quality flags triggered by lightning strikes were produced during the O3 run; they
 695 proved useful in a test aiming at filtering out part of the false-alarm triggers found by
 696 a real-time transient GW search [19]. Further studies are planned during the O4 run
 697 preparation.

698 6.3. Cosmic muons

699 Ground-based GW detectors are constantly passed through by *muons*, produced by
 700 the interaction of cosmic rays with Earth's atmosphere [55]. These energetic charged
 701 particles can interact with the detector test masses and constitute an additional source
 702 of noise, as addressed in the literature since the first prototypes of resonant mass GW
 703 detectors [56, 57, 58, 59].

704 We report here the preliminary results on the first measurement of potential effects of
 705 these muons on the Virgo detector noise. Further result can be found in [60]. This study
 706 has been carried out by means of about 17 days, at the end of the O3b run, of joint data
 707 acquisition of Virgo and a muon telescope designed by the IP2I laboratory [61], installed
 708 in the CEB close to the beam splitter mirror. Two kind of tests have been performed.
 709 In the first one, we have evaluated whether the rate of muons in the correspondence of
 710 GW candidate events was larger than the reference values of the period: we have found
 711 no statistical evidence of an excess of muons in correspondence of these triggers. In the
 712 second test, we have estimated the correlation of this rate with the rate of glitches in
 713 Virgo noise. Figure 27 shows the time series corresponding to the rates of glitches and
 714 muons, averaged on strides of 30 minutes. Here, a correlation is clearly evident. This
 715 is actually not surprising, for the number of the muons arriving at ground being highly
 716 dependent on air density and ultimately on parameters like atmospheric pressure and
 717 temperature. These quantities are also witnesses of the weather conditions, which in
 718 turn can determine an increase of the detector noise, as we have commented in Sec. 5.1.
 719 Therefore, both the variations of these rates share the same main cause, which explain

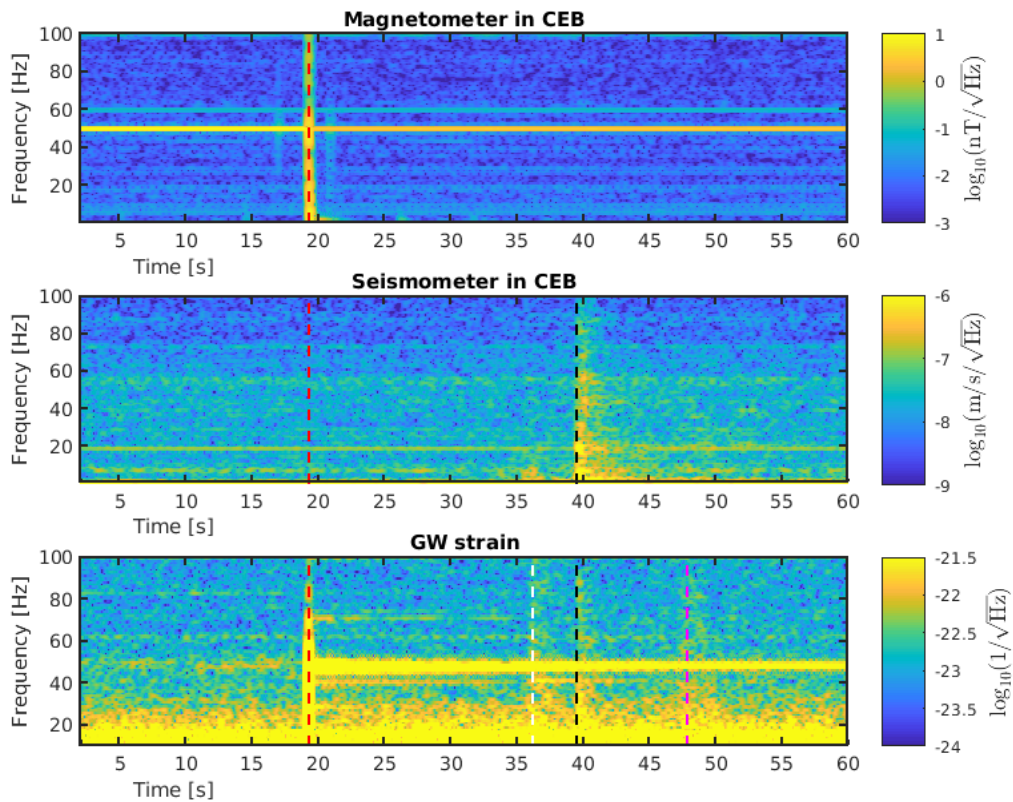


Figure 26: Impact on the Virgo environment and detector of one lightning strike which occurred 6 to 10 km away from Virgo buildings on November 15, 2019 at 23:25:51 UTC. The spectrograms of a few relevant signals are shown. (Top) A prompt magnetic transient is detected by magnetometers at the time of the event, marked by the red vertical line. (Middle) A few seconds later, a seismic (and acoustic, not shown) transient is detected in the central experimental area, marked by the black vertical line. The bottom spectrogram shows the reconstructed GW strain during the same time interval. The red vertical line marks the lightning strike occurrence, the black, magenta and white vertical lines mark the occurrence of seismic transients detected in the CEB, NEB and WEB, respectively.

720 their large correlation. Once the effects of the atmospheric conditions are removed via
 721 a regression analysis, the residuals exhibit no significant correlation.

722 7. Outlook and prospects for O4

723 The Virgo detector performances are affected by external environment conditions; in
 724 particular, seismic noise, earthquakes, bad weather, magnetic noise and lightnings have
 725 an impact on the detector sensitivity or duty cycle. The main coupling mechanisms are:

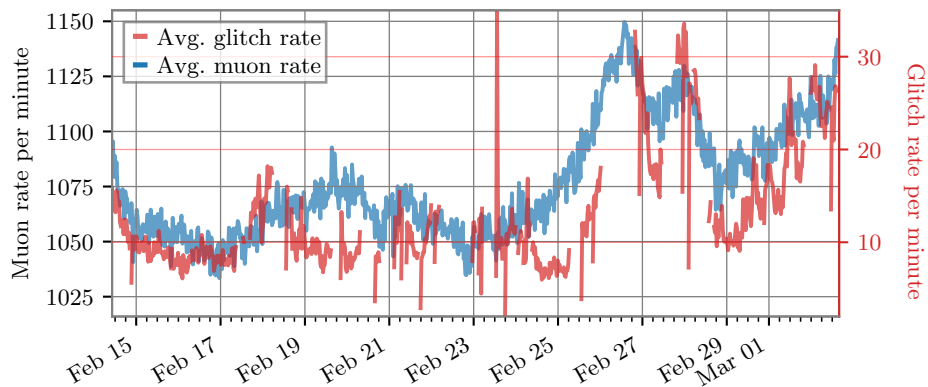


Figure 27: Correlation between muon and glitch rates. The blue line represents the time series of the average rate per minute of muons while the red one is the time series of the rate per minute of glitches with $\text{SNR} > 4.5$ and frequency at peak in $[10, 4096]$ Hz as identified by the Omicron pipeline [40]. Gaps in the latter correspond to periods when the detector was not taking data.

726 direct excitation of suspended mirrors, vibration of experimental buildings, shaking of
 727 benches hosting auxiliary optical systems, disturbances on critical electronic equipment,
 728 scattered light.

729 If the detector control system is able to manage the effect of a disturbance, the
 730 interferometer can remain at its working point with a reduced sensitivity. Otherwise
 731 the global control gets lost and the procedure to recover it has to be started again from
 732 the beginning, thus impacting on the duty cycle – see Appendix A.

733 In this work we reported the results of the analysis of such events during the O3 run.
 734 Thanks to the large amount of data collected, we were able to perform a careful statistical
 735 analysis of the impact of several kinds of external disturbances.

736 The results confirm that the Virgo detector is a very robust apparatus. The sensitivity
 737 reduction due to anthropogenic seismic noise is very low: less than 2% in terms of BNS
 738 range. Also the degradation due to the wind is limited: it appears only for wind speeds
 739 larger than 25 km/h, reaching a sensitivity reduction as large as 10% only for very high
 740 speed (larger than 50 km/h).

741 In these cases, the sensitivity reduction is due to an increased noise at low frequency as
 742 well as to the appearance of short high frequency glitches. In few cases, such kind of
 743 noise was indirectly originated by lightnings.

744 Both microseism and wind have an impact on the detector duty cycle, since the
 745 increasing correction signals acting on the mirror during bad weather can saturate,
 746 finally resulting to a control loss. It results that the Virgo detector global control is
 747 more robust against microseism while it is less effective against strong wind.

748 The analysis of control losses during O3 confirms that earthquakes are a relevant source

749 of these. The Seismon framework, useful to keep the detector in a safe state to try to
750 avoid loosing its control during such events, was used during the whole O3 run and it
751 is now being upgraded for the next scientific run.

752 An upgrade of the environmental monitoring system is in progress to better face the
753 influence of external disturbances: installation of a new lightning detector in the central
754 area; installation of two additional weather stations at the end buildings to monitor local
755 wind gusts; and the installation of more sensitive accelerometers on locations prone to
756 light scattering (viewports, external optical benches, etc.).

757 These actions, together with several other upgrades of the Virgo detector, already
758 performed or presently in progress, will have a crucial role for the success of the next
759 scientific run O4, which is expected to start at the end of 2022.

760 Acknowledgements

761 **October 2020 version** – <https://tds.virgo-gw.eu/q1/?c=15940>

762 The authors gratefully acknowledge the Italian Istituto Nazionale di Fisica Nucleare
763 (INFN), the French Centre National de la Recherche Scientifique (CNRS) and the
764 Netherlands Organization for Scientific Research, for the construction and operation
765 of the Virgo detector and the creation and support of the EGO consortium. The
766 authors also gratefully acknowledge research support from these agencies as well as by
767 the Spanish Agencia Estatal de Investigación, the Consellera d’Innovació, Universitats,
768 Ciència i Societat Digital de la Generalitat Valenciana and the CERCA Programme
769 Generalitat de Catalunya, Spain, the National Science Centre of Poland and the
770 Foundation for Polish Science (FNP), the European Commission, the Hungarian
771 Scientific Research Fund (OTKA), the French Lyon Institute of Origins (LIO),
772 the Belgian Fonds de la Recherche Scientifique (FRS-FNRS), Actions de Recherche
773 Concertées (ARC) and Fonds Wetenschappelijk Onderzoek – Vlaanderen (FWO),
774 Belgium. The authors gratefully acknowledge the support of the NSF, STFC, INFN,
775 CNRS and Nikhef for provision of computational resources.

776 *We would like to thank all of the essential workers who put their health at risk during*
777 *the COVID-19 pandemic, without whom we would not have been able to complete this*
778 *work.*

779 Appendix A. Study of the control losses during O3

780 The Virgo detector needs to be controlled accurately in order to be sensitive to
781 gravitational-wave signals [17, 18]. Schematically, there is an automated procedure [19]
782 that brings the instrument from an initial state where the optics and the laser are
783 controlled independently one from another, to the nominal state where the different

784 optical cavities are jointly resonant and the interferometer itself is used as a length
 785 etalon to control further the laser frequency. That procedure typically takes about
 786 15-20 minutes and requires 1-2 attempts to complete. Then, the global control of the
 787 detector is kept as long as possible, with feedback loops maintaining Virgo at its nominal
 788 working point. When that control is lost for whatever reason, data taking stops and
 789 the control acquisition procedure has to be started again. This leads to a decrease of
 790 the instrument duty cycle and can cause transient gravitational waves to be missed.
 791 Therefore, it is important to find out the causes of the control losses and to use this
 792 information to improve the feedback systems and make them more robust.

793 As explained in Sec. 4 above, a global study of the control losses was needed to be
 794 able to extract those likely due to earthquakes. It was decided to focus on the 601
 795 control losses that occurred during O3 while the detector was taking data in nominal
 796 conditions (Science mode), to be sure that no particular human action was happening
 797 on the instrument at any of these times. Related to the duration of the O3 run (about
 798 11 months) and to the duty cycle of the Virgo detector (about 75%), this corresponds
 799 to about 1 control loss every 10 hours of data taking on average. And, in reality,
 800 uninterrupted data taking stretches could be much longer as control losses usually cluster
 801 in time when a particular problem impacts the detector.

802 The first part of the study was to define the time the control loss occurred for each of
 803 these events. For that, we have used three different Virgo DAQ channels.

- 804 • Two fast channels, sampled at 10 kHz: `ARM_POWER`, latching when the power stored
 805 in the kilometric arm cavities goes below some threshold, meaning that they are
 806 not resonant anymore; `DARK_FRINGE_SHUTTER`, triggered when the fast shutter
 807 protecting the dark fringe photodiodes from an excess of light [2] closes.
- 808 • One slow channel, sampled at 1 Hz: `AUTOMATION_STATUS`, monitoring the global
 809 status of the detector, as seen by the automation process that steers the instrument.

ARM_POWER	DARK_FRINGE_SHUTTER	AUTOMATION_STATUS	Total
14	559	28	601

Table A1: Number of control losses in Science mode witnessed first by each DAQ channel used to time accurately control losses. As expected, the two fast channels are by far those that detect a control loss first. Most of the time the fast shutter protecting the dark fringe photodiodes closes before the arm power loss gets large enough to trigger the other fast channel.

810 The time of a control loss is defined as the earliest time one of these three switches flips
 811 from its nominal value to the value corresponding to an uncontrolled detector. Most of
 812 the time, as expected, the fast channels are the first ones to latch. And they do almost
 813 simultaneously, given that the cavity resonance losses are all connected. Though, in

814 practice, the dark fringe shutter closes almost always before the cavity arm power has
 815 decreased below its nominal threshold. In addition there are a few cases for which the
 816 central automation system triggers first a shutdown of the detector global control, either
 817 because it has detected an issue or because it has received a manual abort request from
 818 the operator on duty. Table A1 shows the breakout of witnesses for the O3 control losses
 819 that occurred while taking Science data.

820 Then, the selected strategy consists in testing several hypothesis in parallel for each
 821 of these events – the main hypothesis investigated are listed in Tabs. A2 and A3 and
 822 documented in the neighbouring text.

823 Various algorithms scanning the data around the control loss have thus been developed,
 824 with the twofold goals of being

- 825 • *complete*: to have as many control losses as possible tagged by at least one control
 826 loss hypothesis;
- 827 • *selective*: to find the right control loss origin as often as possible.

828 Achieving (close to) completeness requires testing many hypothesis, while a profusion
 829 of algorithms could be detrimental to the selectivity of the method. Therefore, the
 830 classification starts with a subset of hypothesis, those that, when identified, certainly
 831 cause a control loss and are also very likely to be the root cause of that particular
 832 event. Obvious examples in that category – called *sure* in the following – are control
 833 losses induced manually by the operator on duty, or hardware problems unambiguously
 834 identified by the real-time monitoring system of the Virgo detector. These control
 835 loss hypothesis are independent by definition and the associated algorithms should be
 836 selective. This has been checked by processing the 601 O3 control losses studied. All
 837 these events have been associated with at most one control loss hypothesis belonging to
 838 the sure category: 24% with one, 76% with none.

Error	Manual	Hardware	Control software	PI	Earthquakes	Total
2	10	92	7	2	30	143 (24%)

Table A2: Sure causes for 143 O3 control losses in Science mode – see text for details.

839 Table A2 provides details about the 143 control losses whose cause has been tagged as
 840 sure, as described above. The dominant class is hardware problems, mainly transient
 841 interruptions of the data flow coming from some suspensions and causing feedback
 842 control systems to fail. The faulty components have been identified and replaced during
 843 the post-O3 shutdown and upgrade phase. Therefore, these problems are not expected
 844 to reoccur during the O4 run. Then, earthquakes are the second most common source
 845 of control losses in the sure category; about three times a month on average. Manual
 846 control losses induced by the operator on shift follow: they are due to the need to switch
 847 from nominal data taking to another task: weekly maintenance, regular calibration or

848 commissioning activity. In O4 and beyond, such control losses should no longer occur as
 849 the procedure will be updated to require leaving Science mode before manually aborting
 850 the control. In 7 cases (only 1% of the total control losses) the source of the event could
 851 be traced to some software problem; 2 more cases were due to human errors.

852 Finally, two control losses are labelled as *PI* for parametric instabilities, an
 853 optomechanical phenomenon due to the interaction between optical and mechanical
 854 modes of the detector and that had been observed at LIGO in 2015 before finally
 855 being seen in Virgo as well in January 2020 [62]. If not mitigated, a PI can make
 856 control systems saturate in a deterministic way (meaning that the saturation will
 857 consistently reoccur as long as the detector remains in a configuration favourable for
 858 its appearance and growth), thus impacting the detector duty cycle. Moreover, it is
 859 impossible to predict exactly what combinations of the instrument parameters will lead
 860 to a PI. Therefore, a dedicated simulation framework has been developed to estimate
 861 the susceptibility of Virgo to PIs during O3, for O4, and beyond [63].

Fast unlocks	Actuation saturation	DARM control inaccuracy	Power loss in sidebands	Arm power asymmetry	Likely missing data	Automation decision	Others	Total
173	85	77	22	4	10	23	64 (11%)	458 (76%)

Table A3: Breakout by category of control losses not tagged as sure. 64 (about 11% of the total number of control losses recorded in Science mode during the O3 Virgo run) control losses have not been accurately classified, either because none of the tested hypothesis seemed to match the recorded data or because too many hypothesis were found matching, making their classification inconclusive. Further studies will be done when pre-O4 control losses data become available, in order to make the current classification more complete.

862 Table A3 describes how the remaining control losses ($\sim 76\%$) have been classified. 11%
 863 of the total remain unclassified, either because none of the hypothesis tested matched,
 864 or because too many did and there was no clear way to find out which one was the root
 865 cause (if identified).

866 The largest category by far (29%) are the so-called *fast unlocks*, events that are
 867 almost instantaneous and occur within the laser injection system, upstream of the
 868 interferometer. Such control losses have been present for years, at rates that strongly
 869 vary over time, ranging from crisis periods lasting some hours to very quiet times. This
 870 past Summer, following detailed investigations of the fast unlock characteristics, this
 871 problem has been finally solved by installing [64] a pigtailed Electro-Optic-Modulator
 872 (EOM) with a larger dynamic, and thus able to compensate the laser frequency glitches
 873 that were found to be the cause of fast unlocks. They have not reoccurred since this new
 874 EOM has been operated.

875 The next five categories are all related to the variety of feedback control systems that are
 876 running in parallel to keep the whole detector at its nominal working point. Improving
 877 the accuracy and the robustness of these systems while making the instrument more
 878 complex and thus more sensitive to the passing of gravitational wave is a permanent
 879 challenge, taken up during each upgrade or commissioning phase.

880 The analysis of the O3 control losses has been made using two independent software
 881 frameworks whose results have been compared: they have been found in good agreement,
 882 in particular for the dominant control loss categories. With the experience gained during
 883 O3, the goals for O4 are to improve the monitoring of the control losses and to reduce
 884 the latency of their analysis. A software framework similar to the Data Quality Reports
 885 (DQR) [19, 65, 66] used to vet in real time the gravitational-wave transient candidates
 886 that are significant enough to trigger a public alert is under development: here control
 887 losses play the role of GW event candidates and the set of checks run to assess the data
 888 quality is replaced by the test of the various hypotheses for control loss. This upgraded
 889 tool will be available to improve the overall performance of the instrument during
 890 the commissioning phase and associated noise-hunting for the new, double-recycled
 891 Advanced Virgo interferometer.

892 References

- 893 [1] Aasi J *et al.* (LIGO Scientific) 2015 *Class. Quant. Grav.* **32** 074001 (*Preprint* 1411.4547)
 894 [2] Acernese F *et al.* (Virgo Collaboration) 2015 *Class. Quant. Grav.* **32** 024001 (*Preprint* 1408.3978)
 895 [3] Akutsu T *et al.* 2021 *Progress of Theoretical and Experimental Physics* **2021** ISSN 2050-
 896 3911 05A102 (*Preprint* [https://academic.oup.com/ptep/article-pdf/2021/5/05A102/](https://academic.oup.com/ptep/article-pdf/2021/5/05A102/38109702/ptab018.pdf)
 897 [38109702/ptab018.pdf](https://doi.org/10.1093/ptep/ptab018)) URL <https://doi.org/10.1093/ptep/ptab018>
 898 [4] Abbott B *et al.* (LIGO Scientific Collaboration, Virgo Collaboration) 2016 *Phys. Rev. Lett.* **116**
 899 061102 (*Preprint* 1602.03837)
 900 [5] Abbott B *et al.* (LIGO Scientific Collaboration, Virgo Collaboration) 2017 *Phys. Rev. Lett.* **119**
 901 161101 (*Preprint* 1710.05832)
 902 [6] Abbott B *et al.* (LIGO Scientific Collaboration, Virgo Collaboration, Fermi GBM, INTEGRAL,
 903 IceCube Collaboration, AstroSat Cadmium Zinc Telluride Imager Team, IPN Collaboration,
 904 Insight-HXMT Collaboration, ANTARES Collaboration, Swift Collaboration, AGILE Team,
 905 1M2H Team, Dark Energy Camera GW-EM Collaboration, DES Collaboration, DLT40,
 906 GRAWITA, Fermi-LAT Collaboration, ATCA, ASKAP, Las Cumbres Observatory Group,
 907 OzGrav, DWF (Deeper Wider Faster Program), AST3 and CAASTRO Collaborations,
 908 VINROUGE Collaboration, MASTER Collaboration, J-GEM, GROWTH, JAGWAR,
 909 CaltechNRAO, TTU-NRAO and NuSTAR Collaborations, Pan-STARRS, MAXI Team,
 910 TZAC Consortium, KU Collaboration, Nordic Optical Telescope, ePESSTO, GROND, Texas
 911 Tech University, SALT Group, TOROS Collaboration, BOOTES Collaboration, MWA,
 912 CALET Collaboration, IKI-GW Follow-up Collaboration, H.E.S.S. Collaboration, LOFAR
 913 Collaboration, LWA, HAWC Collaboration, Pierre Auger Collaboration, ALMA Collaboration,
 914 Euro VLBI Team, Pi of Sky Collaboration, Chandra Team at McGill University, DFN,
 915 ATLAS Telescopes, High Time Resolution Universe Survey, RIMAS, RATIR, SKA South
 916 Africa/MeerKAT) 2017 *Astrophys. J. Lett.* **848** L12 (*Preprint* 1710.05833)
 917 [7] Abbott B *et al.* (LIGO Scientific Collaboration, Virgo Collaboration) 2019 *Phys. Rev. X* **9** 031040
 918 (*Preprint* 1811.12907)

- 919 [8] Abbott R *et al.* (LIGO Scientific Collaboration, Virgo Collaboration) 2021 *Phys. Rev. X* **11** 021053
920 (*Preprint* 2010.14527)
- 921 [9] Abbott R *et al.* (The LIGO Scientific Collaboration, the Virgo Collaboration and the KAGRA
922 Collaboration) 2021 *arXiv e-prints (Preprint* 2111.03606)
- 923 [10] Abbott R *et al.* 2021 *The Astrophysical Journal Letters* **913** L7 URL [https://doi.org/10.3847/
924 2041-8213/abe949](https://doi.org/10.3847/2041-8213/abe949)
- 925 [11] Abbott R *et al.* (LIGO Scientific Collaboration and Virgo Collaboration) 2021 *Phys. Rev. D*
926 **103**(12) 122002 URL <https://link.aps.org/doi/10.1103/PhysRevD.103.122002>
- 927 [12] Fiori I *et al.* 2020 *Galaxies* **8** ISSN 2075-4434 URL <https://www.mdpi.com/2075-4434/8/4/82>
- 928 [13] Nguyen P *et al.* 2021 *Classical and Quantum Gravity* URL [http://iopscience.iop.org/
929 article/10.1088/1361-6382/ac011a](http://iopscience.iop.org/article/10.1088/1361-6382/ac011a)
- 930 [14] Washimi T *et al.* 2021 *Classical and Quantum Gravity* **38** 125005 URL [https://doi.org/10.
931 1088/1361-6382/abf89a](https://doi.org/10.1088/1361-6382/abf89a)
- 932 [15] Punturo M *et al.* 2010 *Classical and Quantum Gravity* **27** 194002 URL [https://doi.org/10.
933 1088/0264-9381/27/19/194002](https://doi.org/10.1088/0264-9381/27/19/194002)
- 934 [16] Acernese F *et al.* 2004 *Astroparticle Physics* **20** 629–640 ISSN 0927-6505 URL [https://www.
935 sciencedirect.com/science/article/pii/S0927650503002603](https://www.sciencedirect.com/science/article/pii/S0927650503002603)
- 936 [17] Acernese F *et al.* 2020 *Astroparticle Physics* **116** 102386 ISSN 0927-6505 URL [https://www.
937 sciencedirect.com/science/article/pii/S0927650519301835](https://www.sciencedirect.com/science/article/pii/S0927650519301835)
- 938 [18] Allocca A *et al.* 2020 *Galaxies* **8** ISSN 2075-4434 URL <https://www.mdpi.com/2075-4434/8/4/85>
- 939 [19] The Virgo Collaboration 2021 *In preparation*
- 940 [20] Barone F, De Rosa R, Eleuteri A, Milano L and Qipiani K 2002 *IEEE Transactions on Nuclear
941 Science* **49** 405–410
- 942 [21] Romero R *et al.* RADIO WAVES below 22 kHz URL <http://www.vlf.it>
- 943 [22] The OpenStreetMap contributors OpenStreetMap URL <https://www.openstreetmap.org>
- 944 [23] Peterson J R 1993 *Open-File Report* URL <http://pubs.er.usgs.gov/publication/ofr93322>
- 945 [24] Koley S *et al.* 2017 *SEG Technical Program Expanded Abstracts* 2946–2950 URL [https://doi.
946 org/10.1190/segam2017-17681951.1](https://doi.org/10.1190/segam2017-17681951.1)
- 947 [25] Longuet-Higgins M S 1950 *Philosophical Transactions of the Royal Society of London. Series A,
948 Mathematical and Physical Sciences* **243** 1–35
- 949 [26] Cessaro R K 1994 *Bulletin of the Seismological Society of America* **84** 142–148
- 950 [27] Flaminio R 2020 Status and plans of the Virgo gravitational wave detector *Ground-based and
951 Airborne Telescopes VIII* vol 11445 ed Marshall H K, Spyromilio J and Usuda T International
952 Society for Optics and Photonics (SPIE) pp 205 – 214 URL [https://doi.org/10.1117/12.
953 2565418](https://doi.org/10.1117/12.2565418)
- 954 [28] Coughlin M *et al.* 2017 *Classical and Quantum Gravity* **34** 044004 URL [https://doi.org/10.
955 1088/1361-6382/aa5a60](https://doi.org/10.1088/1361-6382/aa5a60)
- 956 [29] Biscans S *et al.* 2018 *Classical and Quantum Gravity* **35** 055004 URL [https://doi.org/10.1088/
957 1361-6382/aaa4aa](https://doi.org/10.1088/1361-6382/aaa4aa)
- 958 [30] Mukund N *et al.* 2019 *Classical and Quantum Gravity* **36** 085005 URL [https://doi.org/10.
959 1088/1361-6382/ab0d2c](https://doi.org/10.1088/1361-6382/ab0d2c)
- 960 [31] Product distribution layer git repository URL <https://github.com/usgs/pdl>
- 961 [32] Berni F *et al.* 2012 The Detector Monitoring System <https://tds.virgo-gw.eu/ql/?c=9005>
- 962 [33] F Berni 2020 DMS help manual <https://tds.virgo-gw.eu/ql/?c=15469>
- 963 [34] 2020 Virgo logbook entry validating the use of the eq mode control configuration to take science-
964 quality data URL <https://logbook.virgo-gw.eu/virgo/?r=48612>
- 965 [35] 2020 Query to the public ingv website URL [http://webservices.ingv.it/fdsnws/event/
966 1/query?starttime=2019-04-01T15%3A00%3A00&endtime=2020-03-27T17%3A00%3A00&
967 minmag=2&maxmag=10&mindepth=-10&maxdepth=1000&minlat=27.0&maxlat=48.0&minlon=
968 -7.0&maxlon=37.5&mininversion=100&orderby=time-asc&timezone=UTC&format=text&
969 limit=10000](http://webservices.ingv.it/fdsnws/event/1/query?starttime=2019-04-01T15%3A00%3A00&endtime=2020-03-27T17%3A00%3A00&minmag=2&maxmag=10&mindepth=-10&maxdepth=1000&minlat=27.0&maxlat=48.0&minlon=-7.0&maxlon=37.5&mininversion=100&orderby=time-asc&timezone=UTC&format=text&limit=10000)

- 970 [36] INGV seismic surveillance center public website URL <http://terremoti.ingv.it>
- 971 [37] Bernardi F *et al.* 2015 *Natural Hazards and Earth System Sciences* **15** 2019–2036 URL <https://nhess.copernicus.org/articles/15/2019/2015/>
- 972
- 973 [38] Early-est: Earthquake rapid location system with estimation of tsunamigenesis URL <http://early-est.rm.ingv.it/warning.html>
- 974
- 975 [39] Welch P 1967 *IEEE Transactions on audio and electroacoustics* **15** 70–73
- 976 [40] Robinet F *et al.* 2020 *SoftwareX* **12** 100620 ISSN 2352-7110 URL <https://www.sciencedirect.com/science/article/pii/S2352711020303332>
- 977
- 978 [41] Canuel B, Genin E, Vajente G and Marque J 2013 *Opt. Express* **21** 10546–10562 URL <http://www.opticsexpress.org/abstract.cfm?URI=oe-21-9-10546>
- 979
- 980 [42] Waş M, Gouaty R and Bonnard R 2021 *Classical and Quantum Gravity* **38** 075020 URL <https://doi.org/10.1088/1361-6382/abe759>
- 981
- 982 [43] Accadia T *et al.* 2010 *Classical and Quantum Gravity* **27** 194011 URL <https://doi.org/10.1088/0264-9381/27/19/194011>
- 983
- 984 [44] Van Heijningen J V *et al.* 2019 *Class. Quant. Grav.* **36** 7 URL <https://iopscience.iop.org/article/10.1088/1361-6382/ab075e>
- 985
- 986 [45] Valdes G, O'Reilly B and Diaz M 2017 *Class. Quant. Grav.* **34** 235009
- 987 [46] Longo A *et al.* 2020 *Class. Quant. Grav.* **37** 145011 (*Preprint* 2002.10529)
- 988 [47] Li H, Li Z and Mo W 2017 *Signal Processing* **138** 146–158 URL <https://www.sciencedirect.com/science/article/pii/S0165168417301135>
- 989
- 990 [48] Cirone A *et al.* 2018 *Rev. Sci.* **89** 114501 URL <https://doi.org/10.1063/1.5045397>
- 991 [49] Schumann W 1952 *Zeitschrift Naturforschung Teil A* **7** 149
- 992 [50] Coughlin M W *et al.* 2018 *Phys. Rev. D* **97**(10) 102007 URL <https://journals.aps.org/prd/abstract/10.1103/PhysRevD.97.102007>
- 993
- 994 [51] Kowalska-Leszczynska I *et al.* 2017 *Classical and Quantum Gravity* **34** 074002 URL <https://doi.org/10.1088/1361-6382/2Faa60eb>
- 995
- 996 [52] Naticchioni L *et al.* 2020 *Journal of Physics: Conference Series* **1468** 012242 URL <https://doi.org/10.1088/1742-6596/1468/1/012242>
- 997
- 998 [53] Sentman, D D 1995 *Schumann Resonances* (CRC Press) chap 11
- 999 [54] Washimi T *et al.* 2021 *Journal of Instrumentation* **16** P07033 URL <https://doi.org/10.1088/1748-0221/16/07/p07033>
- 1000
- 1001 [55] Maurin D, Melot F and Taillet R 2014 *Astronomy & Astrophysics* **569** A32
- 1002 [56] Beron B L and Hofstadter R 1969 *Phys. Rev. Lett.* **23**(4) 184–186 URL <https://link.aps.org/doi/10.1103/PhysRevLett.23.184>
- 1003
- 1004 [57] Amaldi E and Pizzella G 1986 *Il Nuovo Cimento C* **9** 612–620
- 1005 [58] Giazotto A 1988 *Physics Letters A* **128** 241–244 ISSN 0375-9601
- 1006 [59] Chiang J, Michelson P and Price J 1992 *Nuclear Instruments and Methods in Physics Research Section A: Accelerators, Spectrometers, Detectors and Associated Equipment* **311** 603–612 ISSN 0168-9002
- 1007
- 1008
- 1009 [60] The ENV team 2021 Future publication about muons separate paper about Virgo and cosmic muons
- 1010
- 1011 [61] Lesparre N *et al.* 2012 *Geoscientific Instrumentation, Methods and Data Systems* **1** 33–42 URL <https://gi.copernicus.org/articles/1/33/2012/>
- 1012
- 1013 [62] Puppò, P for the Virgo Collaboration 2021 Parametric Instability Observation in Advanced Virgo second European Physical Society Conference on Gravitation: measuring gravity URL https://agenda.infn.it/event/26098/contributions/132480/attachments/83185/109525/EPS_Online2021_PI.pdf
- 1014
- 1015
- 1016
- 1017 [63] Cohen D *et al.* 2021 Towards optomechanical parametric instabilities prediction in ground-based gravitational wave detectors (*Preprint* 2102.11070)
- 1018
- 1019 [64] 2021 Virgo logbook entry reporting the installation of the new pigtailed eom URL <https://logbook.virgo-gw.eu/virgo/?r=52813>
- 1020

- 1021 [65] The LIGO Scientific Collaboration and The Virgo Collaboration 2018 Data Quality Report User
1022 Documentation <https://docs.ligo.org/detchar/data-quality-report>
- 1023 [66] Davis D *et al.* 2021 *Classical and Quantum Gravity* **38** 135014 URL [https://doi.org/10.1088/](https://doi.org/10.1088/1361-6382/abfd85)
1024 1361-6382/abfd85